Microphysical and thermodynamic retrievals in deep convective clouds using polarimetric radar measurements and spectral cloud models with explicit treatment of aerosol impact on convective processes (DE-SC0014295)

FINAL REPORT

12 January 2020

Dr. Alexander Ryzhkov, Principal Investigator

Cooperative Institute for Mesoscale Meteorological Studies (CIMMS) / University of Oklahoma

120 David L Boren Blvd

Norman, OK 73072

405-325-6624

Alexander.Ryzhkov@noaa.gov

Dr. Alexander Khain, Co-Principal Investigator (Contractor)

The Hebrew University of Jerusalem, Israel

Dr. Scott Giangrande, Co-Principal Investigator (Collaborator)

Brookhaven National Laboratory

KEYWORDS: Spectral (bin) cloud models, aerosols, microphysical and thermodynamic radar retrievals, polarimetric weather radar

OBJECTIVE: Project goals:

(1) Developing novel techniques for microphysical and thermodynamic retrievals in convective storms using polarimetric radar data.
(2) Investigating the impact of aerosol processes on the properties of convective systems using advanced cloud models with spectral microphysics and polarimetric radar observations.
(3) Examining multifrequency polarimetric ARM radar data to improve microphysical parametrizations in the models, develop new radar retrieval methodologies, and validate their efficiency.

I. Developing novel techniques for microphysical and thermodynamic retrievals in convective storms using polarimetric radar data.

Various techniques for microphysical retrievals and quantification of rain and ice / snow amounts and fluxes using polarimetric radar data have been developed during the project. These are described in the monograph of A. Ryzhkov and D. Zrnic "Radar Polarimetry for Weather Observations" (2019) and in journal articles by Carlin et al. (2017) and Bukovcic et al. (2017, 2019).

1.1. Radar microphysical retrievals in rain and rain mixed with hail

Rain microphysical retrievals include determination of rain rate R, liquid water content LWC, mean volume diameter D_m, normalized concentration N_w, and total concentration of raindrops N_t. A novel method for estimation of rain rate based on the combination of specific attenuation A and specific differential phase K_{DP} was suggested by Ryzhkov et al. (2014) and proved to be the best rainfall estimation algorithm at S band (Wang et al. 2019; Cocks et al. 2019). New routines for retrieval of the key parameters of the raindrop spectrum LWC, D_m, N_w, and N_t have been developed and utilized to evaluate model simulations of the MC3E May 20, 2011 storm and investigate the impact of aerosols on a life cycle of convective cells in the Houston area (Fridlind et al. 2017; Hu et al. 2019b). The latter was a pilot project preceding the future DOE ARM deployment in the same region as part of the TRacking Aerosol Convection interactions ExpeRiment (TRACER) planned in 2021 – 2022. Analysis of several convective storms observed with the Houston WSR-88D radar shows apparent land / sea contrasts in terms of D_m and N_w : D_m is consistently higher and N_w is lower over the land than over Gulf of Mexico which may be related to the substantial difference between aerosol concentration in the atmosphere above the sea and in a heavily polluted inland area near Houston.

Limitations of using the standard Z – LWC and Z – IWC relations for estimation of the liquid and ice water contents (LWC and IWC respectively) have been examined in the study of Carlin et al. (2016). A novel technique for the LWC and IWC retrievals in the mixture of rain and graupel / hail using polarimetric radar variables Z_{DR} and K_{DP} is proposed based on simulations of deep convective storms using cloud models with spectral bin microphysics coupled with a sophisticated polarimetric radar operator. The models used are a one-dimensional model of melting hail (Ryzhkov et al. 2013) and the two-dimensional Hebrew University Cloud Model (HUCM).

1.2. Radar microphysical retrievals in ice and snow

In deep convection, high-resolution numerical simulations with spectral bin microphysics and a polarimetric forward operator reveal a strong spatial association between convective updrafts and the columns of Z_{DR} and K_{DP} and demonstrate the utility of examining the structure and evolution the Z_{DR} and K_{DP} columns for assessing updraft strength and development. An automated Z_{DR} column algorithm has been designed to provide diagnostic and prognostic information pertinent to convective storm nowcasting (Snyder et al. 2015). An example of temporal evolution of Z and Z_{DR} throughout a life cycle of an isolated convective cell observed in the Houston area is shown in Fig. 1. Initial radar echo aloft is characterized by low Z and very high Z_{DR}, particularly near the bottom of the echo, which indicates initial formation and sedimentation of very large raindrops via coalescence process. Further in a life cycle, Z increases and Z_{DR} tends to decrease while both Z and Z_{DR} cores descend to the surface. Such evolution takes only 15 – 20 min.

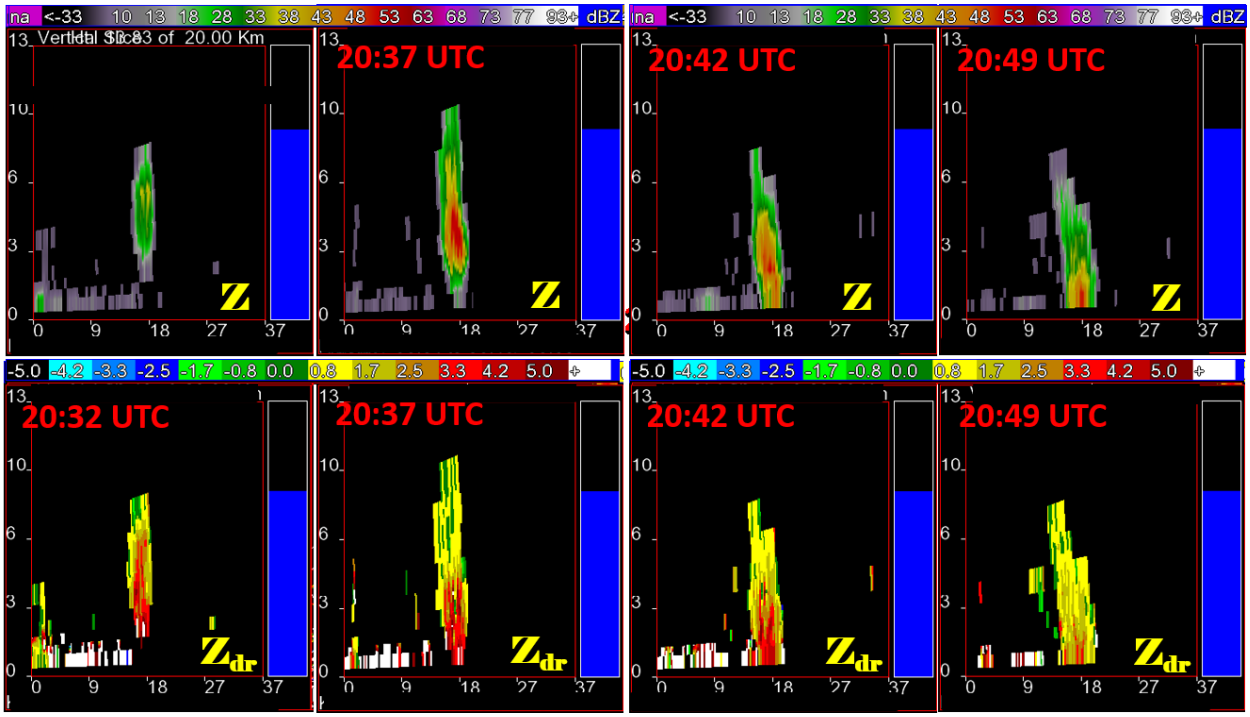

Fig. 1 An example of temporal evolution of Z and Z_{DR} throughout a life cycle of an isolated convective cell observed in the Houston area.

In the paper of Fridlind et al. (2019), the focus is on the K_{DP} columns which manifest initial growth of the precipitation-size mixed-phase hydrometeors in the updrafts and their further sedimentation as a precipitation shaft. Descending K_{DP} columns initially stretching above the freezing level indicate convective downdrafts containing melting hail if K_{DP} values are sufficiently high. Such downdrafts are often associated with cold pools of descending air which may trigger strong microbursts near the surface. An example of a descending K_{DP} column is shown in Fig. 2 for the microburst case documented by the KBMX WSR-88D radar in Alabama.

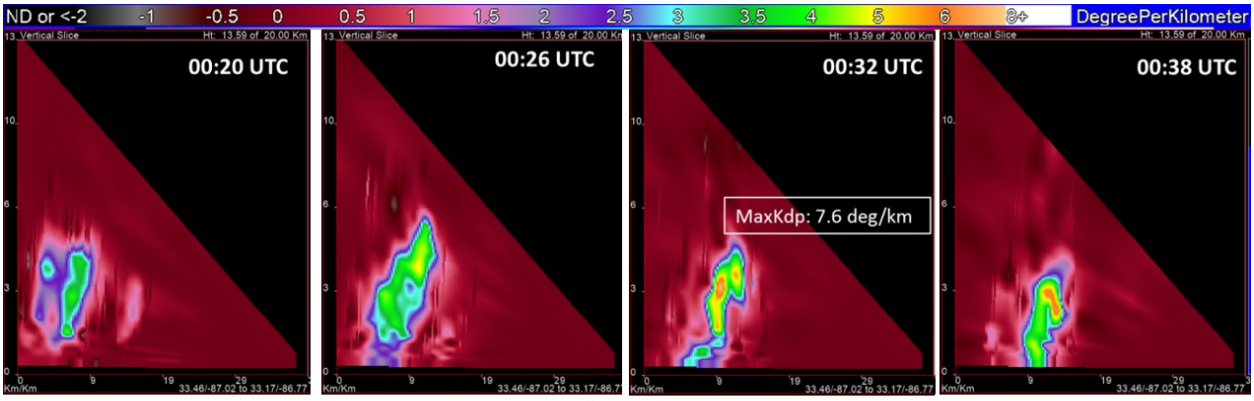

Fig. 2 An example of a descending K_{DP} column for the microburst case documented by the KBMX WSR-88D radar in Alabama on 10 June 2018.

Another new development is the technique for estimation of depolarization ratio (DR) using weather radars with simultaneous transmission / reception which do not directly measure DR (Ryzhkov et al. 2017). It is suggested to address this deficiency by using either special signal processing routine or a combination of two routinely measured polarimetric variables, differential reflectivity Z_{DR} and cross-correlation coefficient ρ_{hv} as proxy of DR. Possible practical implications of using DR include the detection of hail and determination of its size above the melting layer, discrimination between various habits of ice aloft, and possible identification and quantification of riming which is associated with the presence of supercooled cloud water. Fig. 3 illustrates convective updraft signatures in a vertical cross-section of a deep convective storm. The updraft is enclosed in white ovals in the fields of Z, Z_{DR}, DR, and ρ_{hv}. It is clear that the DR column is taller than the Z_{DR} column and yields much better representation of the convective updraft.

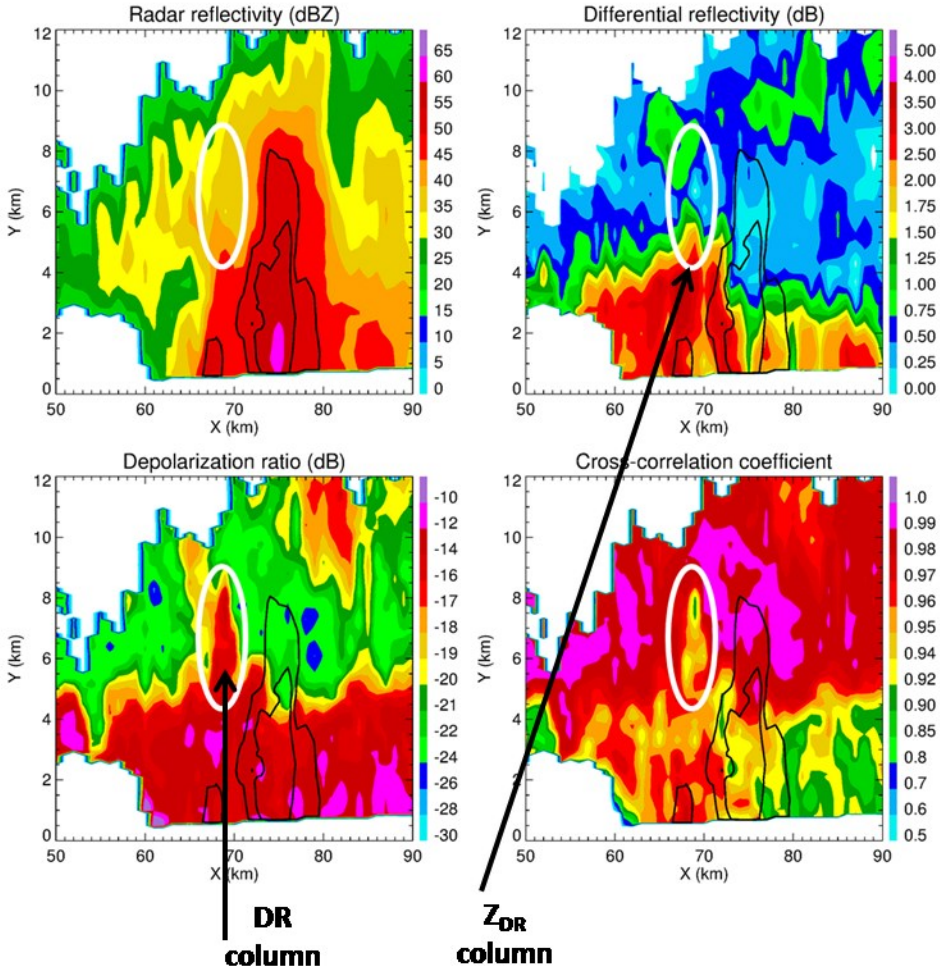

Fig. 3. Convective updraft signatures in a vertical cross-section of a deep convective storm. The updraft is enclosed in white ovals in the fields of Z, Z_{DR}, DR, and ρ_{hv}.

Substantial progress has been achieved in the polarimetric radar microphysical retrievals in ice and snow. The following novel polarimetric relations for estimation of ice water content IWC, mean volume diameter D_m, and total concentration of ice particles N_t have been suggested (Ryzhkov and Zrnic 2019):

$$IWC = 4.0\,10^{-3}\,\frac{K_{DP}\lambda}{1 - Z_{dr}^{-1}} \quad , \qquad (1)$$

$$D_m = -0.1 + 2.0\left(\frac{Z_{DP}}{K_{DP}\lambda}\right)^{1/2} \quad , \qquad (2)$$

$$\log(N_t) = 0.1Z(dBZ) - 2\log\left(\frac{Z_{DP}}{K_{DP}\lambda}\right) - 1.11 \qquad (3)$$

where $Z_{DP} = Z_h - Z_v$ is the reflectivity difference in mm^6m^{-3}, Z_{dr} is the differential reflectivity in linear scale, and λ is the radar wavelength in mm. In (1) – (3), IWC is expressed in g m^{-3}, D_m is in mm, and N_t is in 1/L. It is important that the estimates (1) – (3) are almost insensitive to the variability of size distributions, shapes, and orientations of ice particles.

One of the primary advantages of using K_{DP} instead of Z for ice retrievals is that K_{DP} is proportional to the first moment of size distribution of ice particles whereas Z is proportional to its fourth moment and is heavily weighted by a few largest ice particles / snowflakes in the size spectrum. This is based on the assumption that the bulk density of ice / snow is inversely proportional to a particle equivolume diameter.

Reliable retrievals of the parameters of size distributions can be made in areas where K_{DP} and Z_{DR} are not close to zero. Therefore, the most accurate retrievals in the cold parts of stratiform clouds are usually produced within the dendritic growth layer (DGL) centered at the -15ºC isotherm where K_{DP} and Z_{DR} reach their maxima. This is important because the bulk of snow precipitation is formed within DGL.

1.3 Illustration of the polarimetric microphysical retrievals for the hurricane Harvey

Polarimetric microphysical retrievals in rain and ice have been used to investigate the microphysical structure of a land-falling hurricane Harvey which hit the Texas coast on August 25, 2017. The eyewalls of hurricanes and their outer rain bands have very different microphysical characteristics and different potentials for flash flooding. The hurricane Harvey exemplifies such difference very well. The composite vertical profiles of LWC / IWC, D_m, and N_t retrieved from the columnar vertical profiles (CVP) of polarimetric radar variables have been generated in the eyewall area of the hurricane and its outer rain bands (Hu et al. 2019b). The centers of the vertical CVP columns are shown in the PPIs of radar reflectivity shown in Fig. 4. The eyewall region was better sampled by the KCPR WSR-88D radar in Corpus Christi (left panel in Fig. 4) whereas the outer rain band was better visible from the perspective of the KHGX WSR-88D radar in Houston (right panel in Fig. 4). The corresponding CVPs in a height vs time format are shown in Figs. 5 and 6.

Comparison of the two CVPs in the eyewall and outer rain band indicates that the eyewall region is characterized by high concentration of very small ice aloft with radar reflectivity generally below 20 dBZ above the melting layer. It is a warm rain mechanism that is primarily responsible for precipitation in the eyewall. In other words, a bulk of rain is formed below the melting layer via coalescence of raindrops, and ice aloft does not play significant role in the precipitation formation. The outer rain band is characterized by noticeably higher radar reflectivity in ice above the melting layer, larger size of ice particles, and lower number concentration. This

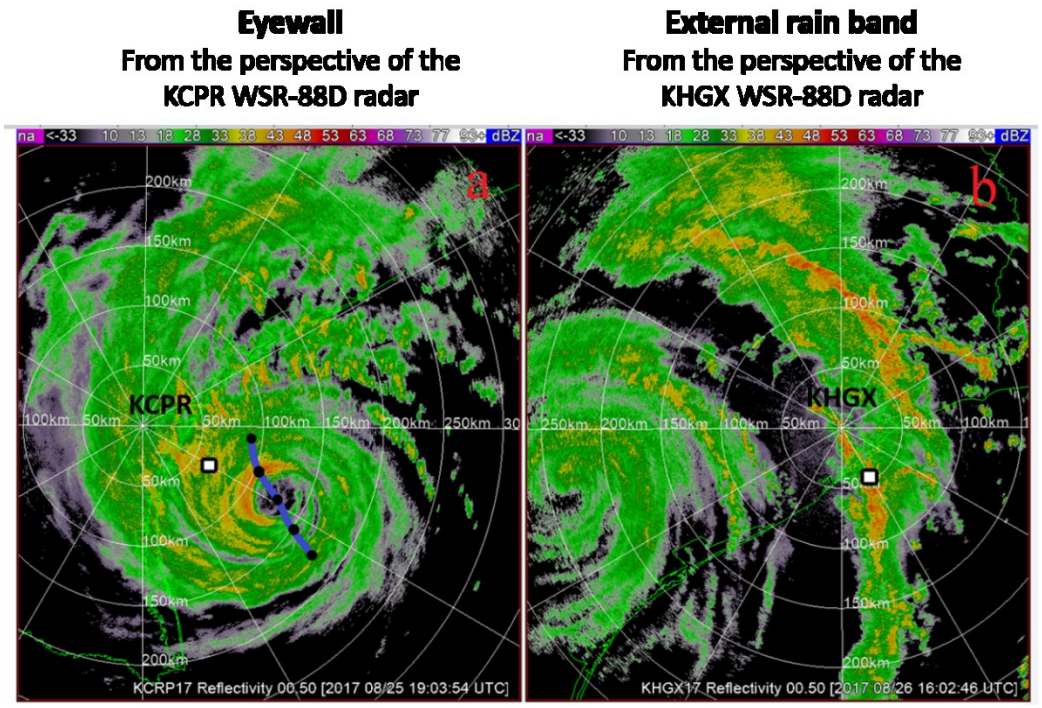

Fig. 4. Radar 0.5-degree reflectivity plan position indicator (PPI) maps. (left panel) Harvey's inner eyewall and (right panel) Harvey's outer rain band. Radar CVP sectors are labeled by the white boxes. The thick blue line with black dots represents a track of the Harvey's eye.

means that good portion of precipitation at the surface is formed via melting of ice. Coexistence of graupel-size ice, ice crystals, and supercooled water lofted in stronger updrafts facilitates electric charge separation and significant lightning discharges in the outer rain band. No lightning was reported in the eyewall region of the hurricane Harvey.

A combination of warm rain generated below the melting layer and rain resulting from the melting of ice originated in stronger convective updrafts makes an outer rain band of the tropical cyclones a more efficient rain producer compared to an eyewall. Extremely heavy rain from the stalled external rain bands has caused most of the flooding during Harvey.

1.4 Thermodynamic retrievals

A new paradigm has been suggested to use polarimetric radar data for thermodynamic retrievals of warming and cooling rates associated with latent heat release and absorption. The rate of change of the environmental temperature at each height can be obtained from relations

$$\frac{dT(z)}{dt} = \frac{1}{c_p \rho_a(z)} \left\{ L_s \int \frac{dm_{i,subl}(D,z)}{dt} N(D,z) dD + L_v \int \frac{dm_{w,evap}(D,z)}{dt} N(D,z) dD + L_f \int \frac{k_a (T - T_p)}{dQ} \frac{dm_{i,melt}(D,z)}{dt} N(D,z) dD \right\} \quad (4)$$

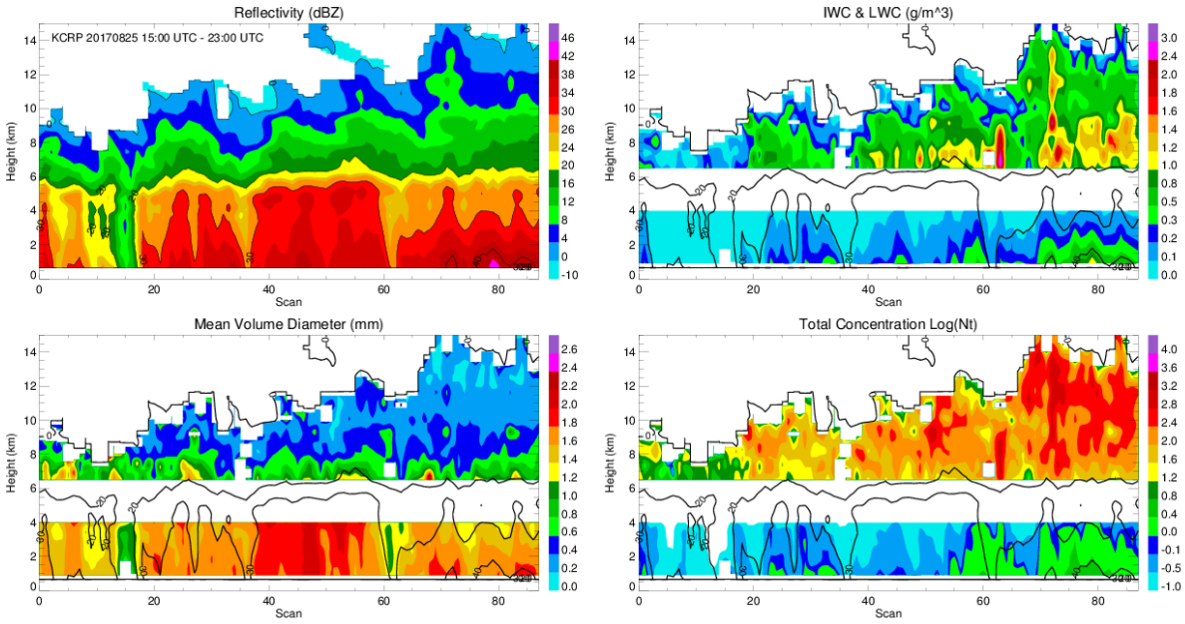

Fig. 5. Radar 0.5-degree reflectivity plan position indicator (PPI) maps. (left panel) Harvey's inner eyewall and (right panel) Harvey's outer rain band. Radar CVP sectors are labeled by the white boxes. The thick blue line with black dots represents a track of the Harvey's eye.

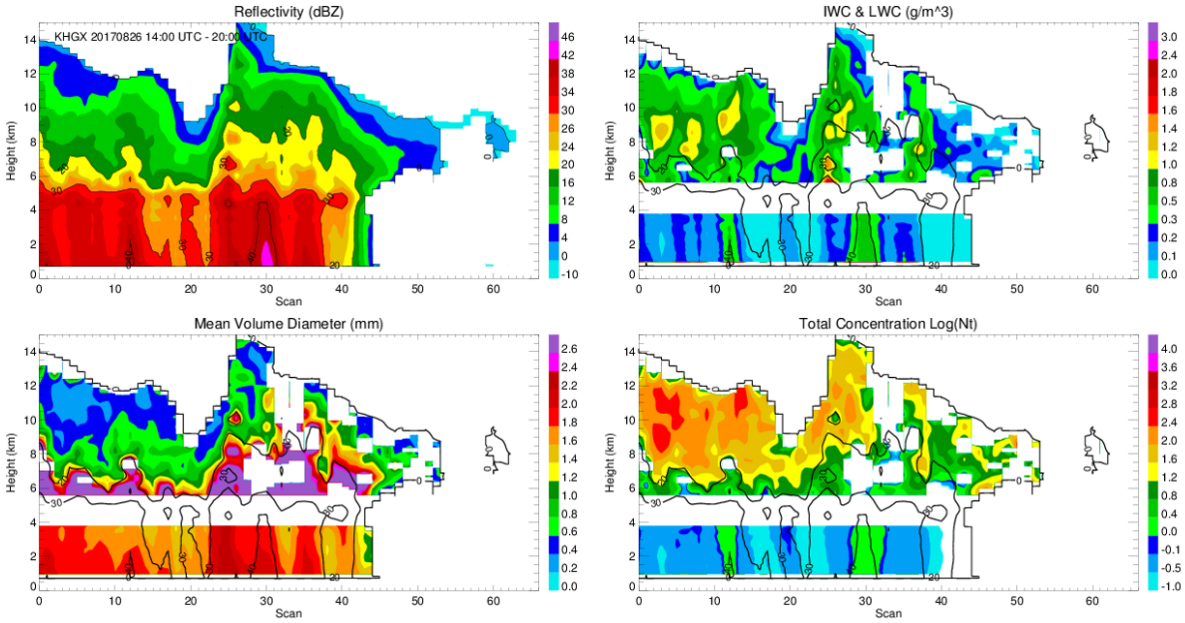

Fig. 6. Columnar vertical profiles (CVPs) of Z, IWC/LWC, D_m, and N_t in the outer rainband of the hurricane Harvey from the perspective of the KHGX WSR-88D radar in Houston. A location of the column base is shown with white rectangle in Fig. 4 (right panel). Overlaid are contours of constant Z following every 10 dBZ.

where N(D,z) is the size distribution of mixed-phase particles, $dm_{i,subl}/dt$ and $dm_{i,melt}/dt$ are the rates of ice loss due to sublimation and melting, $dm_{w,evap}/dt$ is the rate of water mass loss due to evaporation, and L_s,

L_v, and L_f are latent heat of sublimation, vaporization, and fusion. A similar equation can be written for the rate of change of the environmental water vapor mixing ratio q_v:

$$\frac{dq_v(z)}{dt} = -\frac{1}{\rho_{a,d}(z)} \int \left[\frac{dm_{i,subl}(D,z)}{dt} + \frac{dm_{w,evap}(d,z)}{dt} \right] N(D,z) dD \qquad (5)$$

The rates dm/dt are determined by environmental thermodynamic variables whereas size distributions of pure rain and pure ice can be retrieved from polarimetric radar measurements as mentioned in the previous subsections and these can be used directly to estimate the warming / cooling rates dT/dt and moistening / drying rates dq_v/dt using Eqs. (4) and (5). If a reliable retrieval of size distributions (SD) from radar measurements is not possible in a full depth of the cloud, then these can be obtained from 1D Lagrangian cloud models initialized with the radar-retrieved SD obtained in areas of reliable retrieval.

Diabatic warming due to condensation of water vapor in a convective updraft is a primary driving force of deep convection. Unfortunately, it is hard to capture the condensation process directly with a radar because of very small size of cloud water droplets usually invisible to the radar. However, a warming rate due to condensation can be better quantified with polarimetric radar markers such as a height of the Z_{DR} column compared to a commonly used radar reflectivity Z or rain rate (also estimated from Z). A conventional way to obtain vertical profiles of latent heat using radar data is to generate a number of vertical warming / cooling rates from the cloud model, store them in lookup tables, and associate each profile with a certain radar parameter (like the height of the 10-dBZ surface) which can be considered as an "index" of the profile.

Our simulations of deep convective storms using the Hebrew University Cloud Model (HUCM) coupled with a polarimetric forward radar operator show that using a height of the 1-dB Z_{DR} surface above the freezing level is much better index of the vertical warming / cooling profiles than any Z-related parameter. This is illustrated in Fig. 7 where these profiles are displayed as functions of the height of the 10-dBZ surface of Z and 1-dB surface of Z_{DR} in a deep hail-bearing convective storm (top panels a and b). It is obvious that the vertical cross section of latent heating retrieved using Z_{DR}-based index (panel e) is in much better agreement with "true" modeled distribution of latent heating (panel c) than the one retrieved using Z-based index (panel d).

Carlin et al. (2017) demonstrated that the use of Z_{DR} columns as proxies for convective updrafts has apparent advantages for radar data assimilation compared to traditional utilization of radar reflectivity Z. One common technique of reflectivity data assimilation is using a cloud analysis, which inserts temperature and moisture increments as well as hydrometeors deduced from Z via empirical relations to induce and sustain updraft circulations. In the study of Carlin et al., the Advanced Regional Prediction System's (ARPS) cloud analysis is modified from its original Z-based formulation to provide moisture and latent heat adjustments based on Z_{DR} columns. According to this approach, positive temperature and moisture perturbations are inserted in the Z_{DR} column areas only, and modest amounts of moisture are removed outside of these locations where Z exceeds 10 dBZ.

In a top panel of Fig. 8, 15-dBZ contours (in grey) of reflectivity and color-shaded Z_{DR} column depths are displayed between 2000 and 2300 UTC in 10-min intervals for the 19 May 2013 storm in Oklahoma. In two bottom panels of Fig.8, the outcomes of the ARPS model runs after assimilation of Z data only (single-pol run, left bottom panel) and Z_{DR} column information (dual-pol run, right bottom column) are compared. The analyzed updraft tracks in a dual-pol run are more coherent and consolidated with less spurious convection than in a single-pol run. The short-term forecast according to a dual-pol run shows a

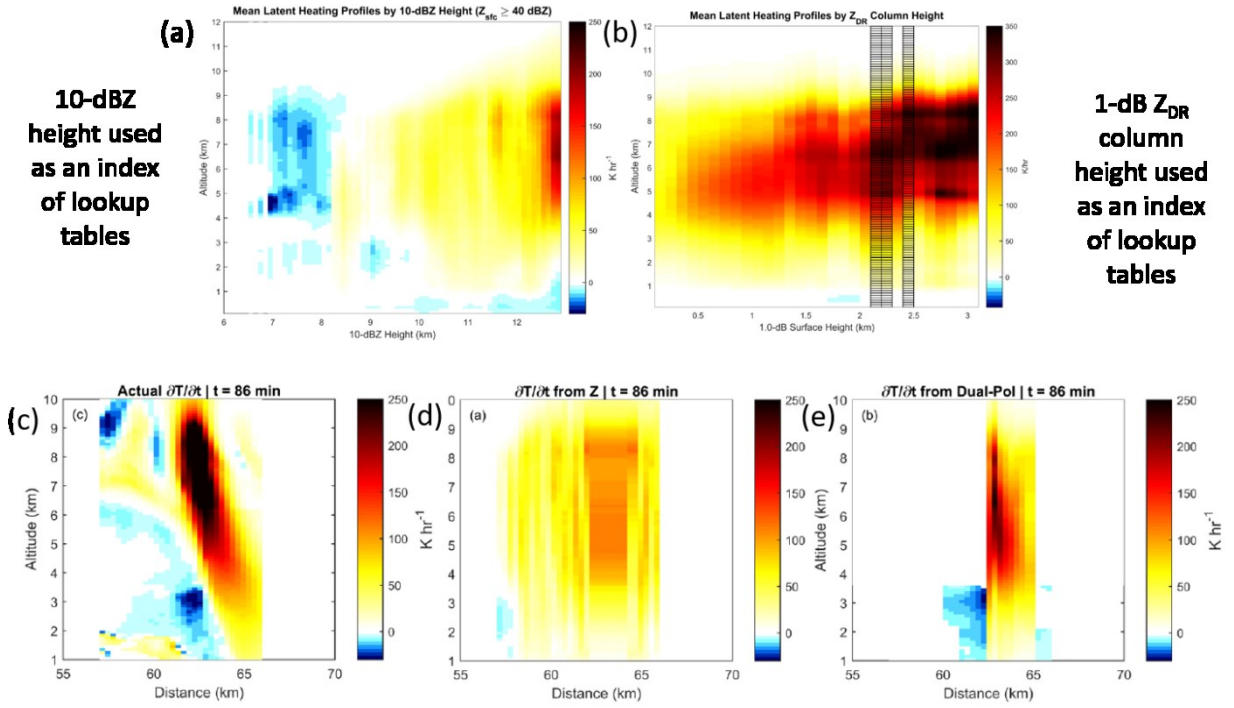

Fig. 7. (a) Mean vertical profiles of warming rate as functions of the height of the Z = 10 dBZ level; (b) Mean vertical profiles of warming rate as functions of the height of the Z_{DR} = 1 dB level; (c) vertical cross section of the warming rate dT/dt obtained from the HUCM simulation of the storm 86 min after the beginning of its life cycle; (d) vertical cross section of the warming rate dT/dt if a height of the Z = 10 dBZ level is used as a lookup table index; (e) vertical cross section of the warming rate dT/dt if a height of the Z_{DR} = 1 dB level is used as a lookup table index. All simulations were performed using HUCM and the polarimetric radar forward operator from Ryzhkov et al. (2011).

reduction in forward speed and northward position bias of the main updrafts, an issue encountered in many storm-scale modeling experiments.

In the melting layer and below, cooling due to melting and evaporation of hydrometeors usually occurs. The cooling rates can be quantified in the framework of simplified 1D Lagrangian models with spectral bin microphysics coupled with forward polarimetric radar operator. In our analyses, we utilized our 1D Lagrangian models for melting hail (Ryzhkov et al. 2013) and melting snow (Carlin and Ryzhkov 2019). A typical vertical profile of cooling rate retrieved from our 1D model below the freezing level for hailstorm is shown in Fig. 9 (right panel). Because this spectral model explicitly and separately treats melting and evaporation of graupel, hail, and rain, their relative contributions to the cooling rate can be estimated (left panel in Fig. 9). As expected, sublimation and melting of graupel are the dominant contributors to the cooling rates within the melting layer and 1 km beneath whereas melting of hail and evaporation of raindrops determine the cooling rates below with evaporation of raindrops originating from complete melting of graupel and hail particles making a largest contribution near the surface. It can be shown that the vertical gradient of K_{DP} is well correlated with the intensity of diabatic cooling in the first two km below the freezing level.

The methodology for estimating cooling rates due to rain evaporation using a 1D spectral bin model and the data collected by dual-polarization radar and micro-rain radar has been developed and

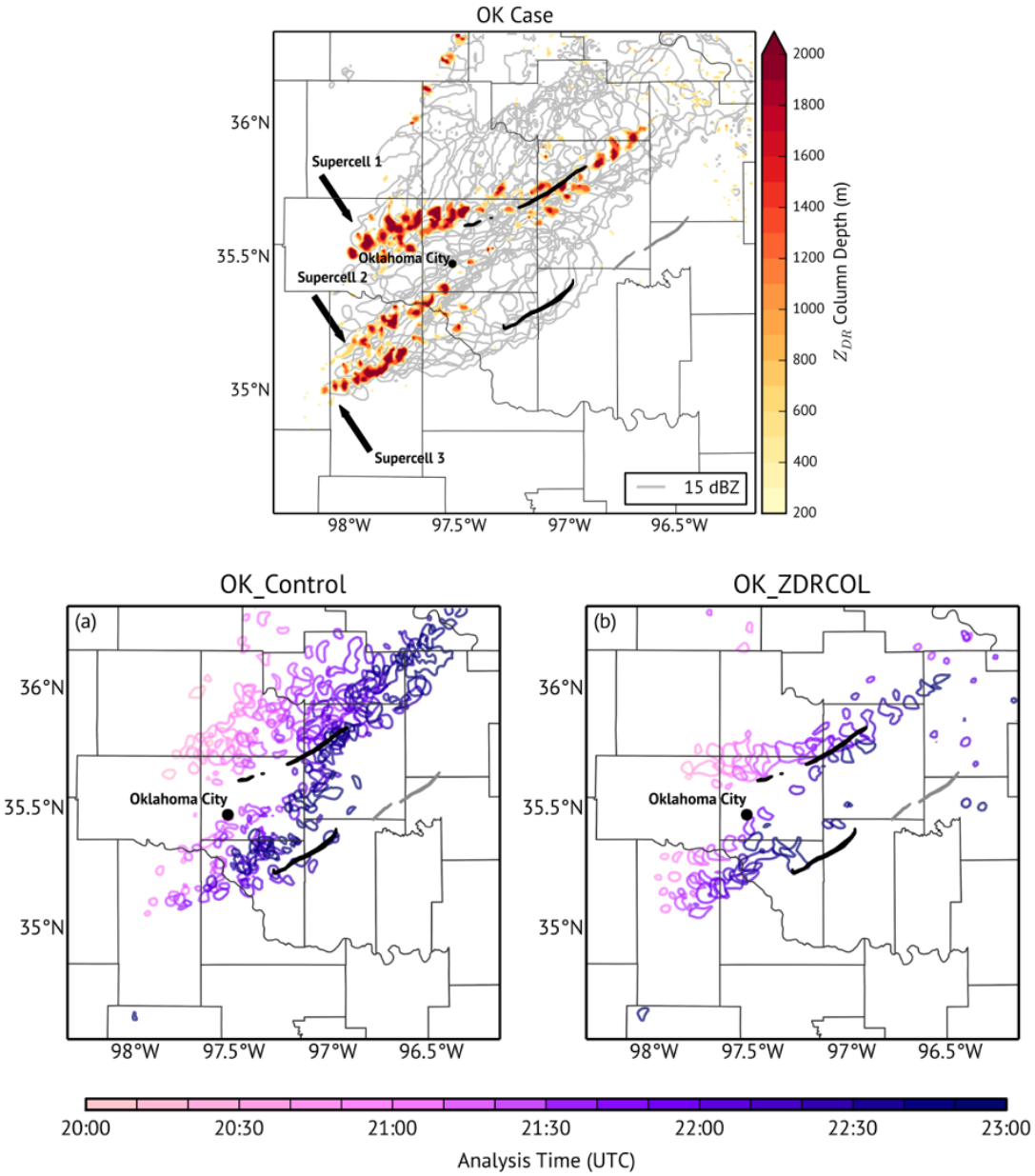

Fig. 8. *Top panel*: composite remapped Z (15-dBZ contour in gray) and analyzed Z_{DR} column depth (color shaded, in m, and defined as the height of the 1-dB surface above the environmental 0ºC level) between 2000 and 2300 UTC in 10-min intervals for the 19 May 2013 storm in Oklahoma. Observed tornado tracks are shown in black and grey, with grey tracks indicating observed tornadoes that fall outside of the period of study. *Bottom panels*: Composite maximum vertical velocity in each grid column for each of post-assimilation analyses from 2000 to 2300 UTC without using polarimetric information (left bottom panel) and utilizing the Z_{DR} column height (right bottom panel). Blue contours show 30 m s^{-1} vertical velocity contour lines with color intensity depending on the analysis time. From Carlin et al. (2017).

demonstrated in the study of Xie et al. (2016). It was shown that polarimetric radar observations can be used to estimate the evaporative cooling rate from the retrieved DSD aloft and the evaporation model.

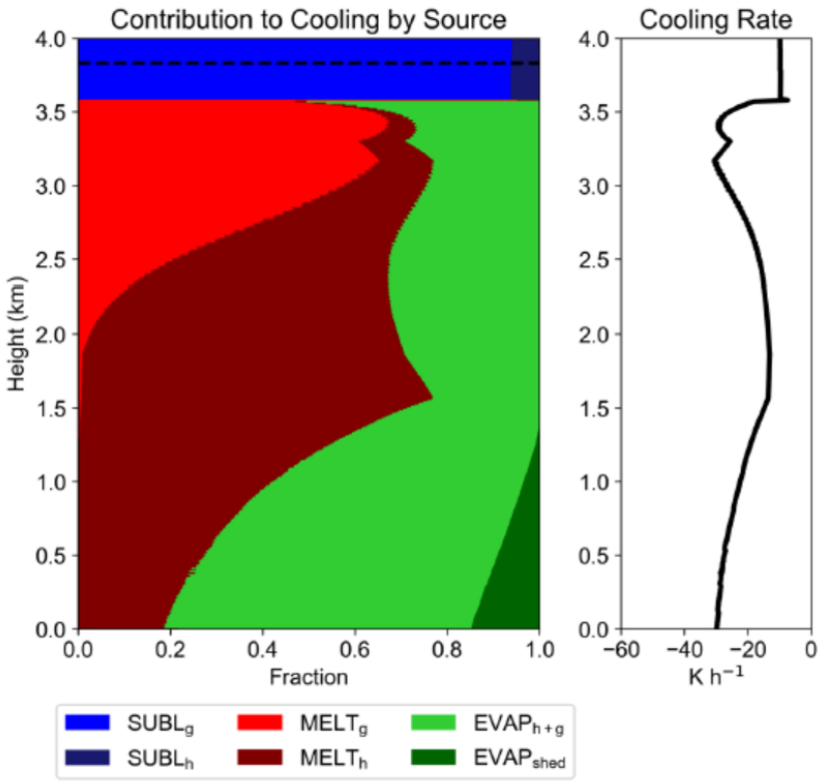

Fig. 9. *Left panel*: relative contributions to the cooling rate by different microphysical processes: sublimation of graupel ($SUBL_g$), sublimation of hail ($SUBL_h$), melting of graupel ($MELT_g$), melting of hail ($MELT_h$), evaporation of rain resulting from melted graupel and hail ($EVAP_{h+g}$), and evaporation of raindrops shed from melting hailstones ($EVAP_{shed}$) as functions of height below the freezing level. *Right panel*: vertical profile of cooling rate resulting from all diabatic processes.

Carlin and Ryzhkov (2019) show that the maximal cooling rate in the melting layer (ML) of stratiform precipitation can be determined from the maximal value of K_{DP} within the ML. This is well illustrated in Fig. 10. The scatterplots of maximal cooling rate vs maximal radar reflectivity Z shows tremendous variability caused by the diversity of size distributions of ice aloft and changes of vertical profiles of temperature and humidity within the ML (top panels in Fig.10) whereas almost perfect linear dependencies of the max(dT/dt) on max(K_{DP}) (bottom panels in Fig. 10) show great promise.

Existing NWP models such as RAP may not adequately treat the impact of the phase transition of hydrometeors on the temperature and moisture perturbations within a storm. This sometimes leads to dramatic failures in predicting the type and amount of precipitation at the surface, especially during cold season as in the "Snowbowl" case on 8 December 2013 when the RAP model didn't predict heavy snowfall during important football game. Fig. 11 presents QVPs of total concentration of snowflakes N_t and their mean volume diameter D_m for this storm retrieved from polarimetric radar data according to Eqs. (2) and (3). The radar-retrieved size distributions at the level of 4 km were used to initialize our 1D spectral bin model (1D SBM) of snow and to determine vertical profiles of cooling and moistening rates following Eqs. (4) and (5). The height vs time plots of these rates are shown in Fig. 12. The moistening rate caused by evaporation of snowflakes was sufficiently high to change relative humidity from less than 25% to 100%

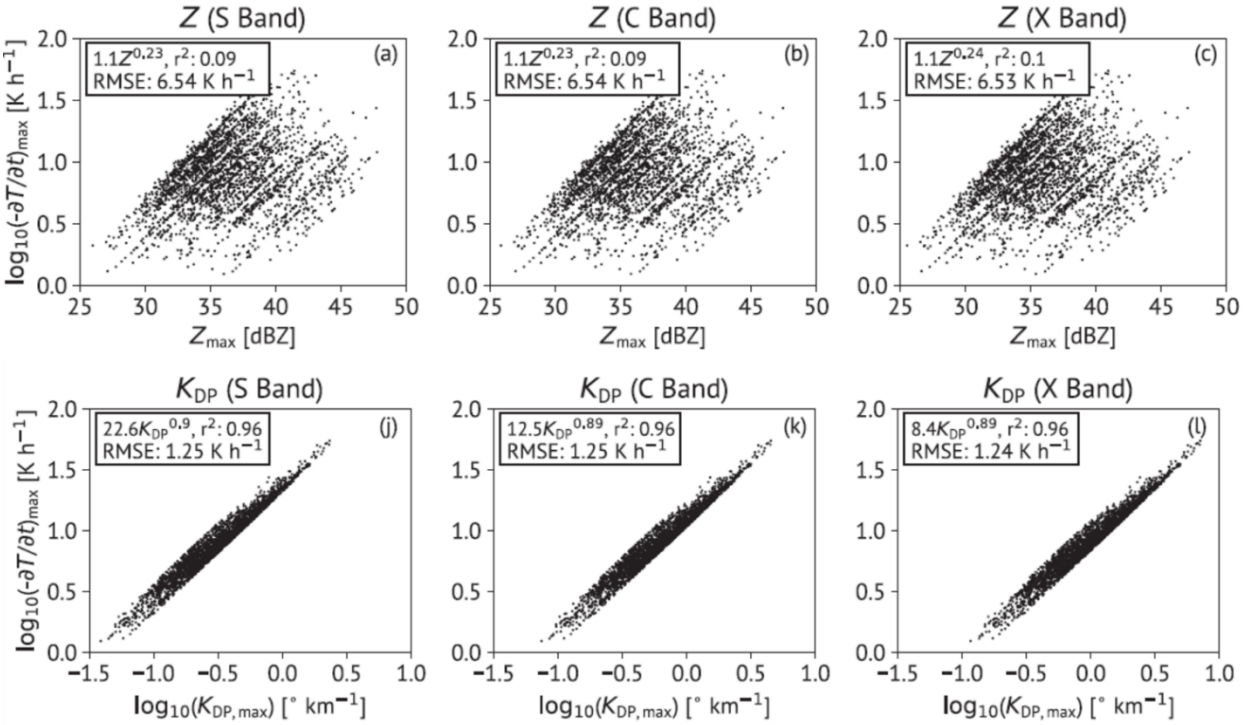

Fig. 10. *Top panels*. Scatterplots of the maximal cooling rate versus maximal Z within the melting layer for various size distributions of snow above the melting layer at S, CX, and X bands. *Bottom panels*: Scatterplots of the maximal cooling rate versus maximal K_{DP} within the melting layer for various size distributions of snow above the melting layer at S, C, and X bands. Adapted from Carlin and Ryzhkov (2019).

during one hour (Fig. 13). This facilitates heavy snowfall that was completely missed by the RAP model (dashed lines in Fig, 13).

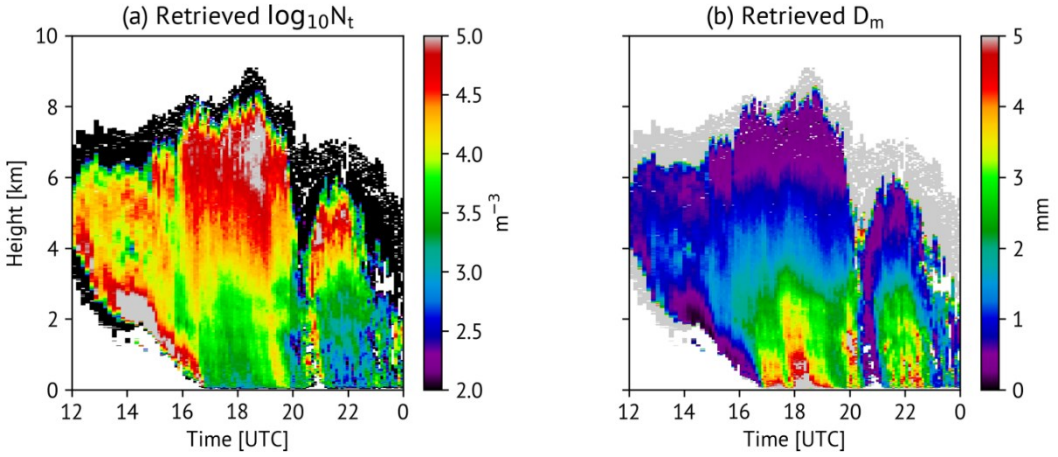

Fig. 11. Vertical profiles of the total number concentration N_t and the mean volume diameter D_m of ice particles retrieved from the polarimetric radar data and presented in a height vs time format for the "Snowbowl" surprise snowstorm on 8 December 2013 in Philadelphia, PA.

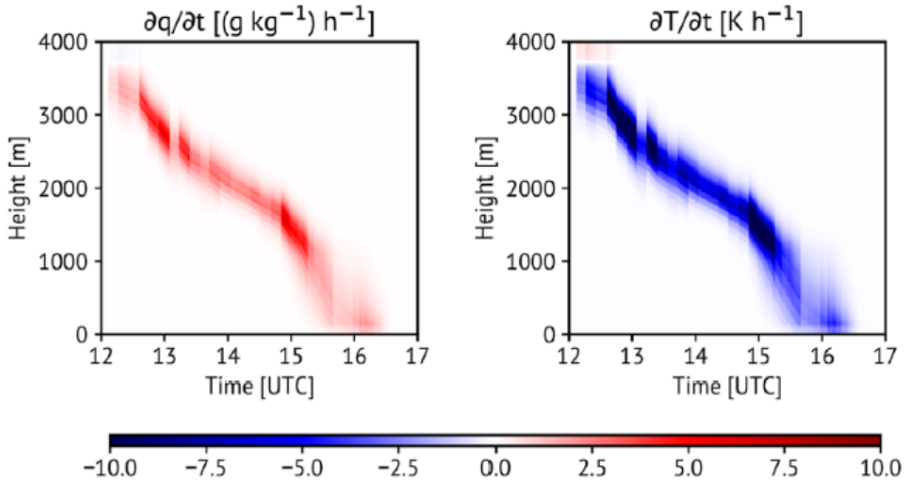

Fig. 12. Vertical profiles of moistening and cooling rates retrieved from 1D SBM in a height vs time format for the "Snowbowl" snow event.

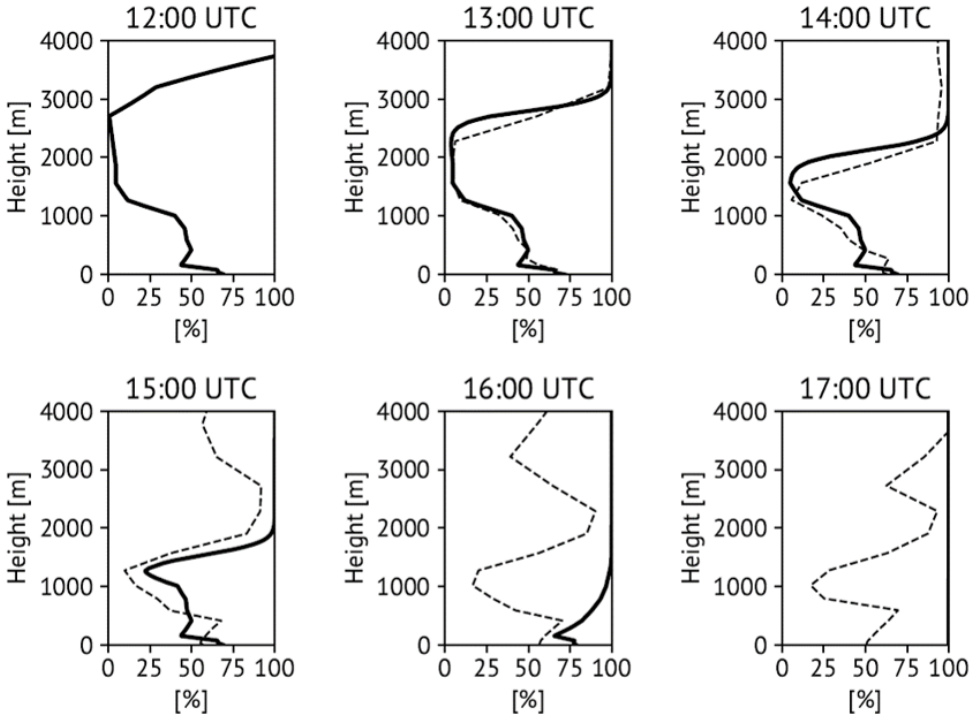

Fig. 13. Vertical profiles of relative humidity retrieved from the RAP model (dashed lines) and 1D spectral bin model (SBM) (solid lines) at different times for the "Snowbowl" snow event.

II. Investigating the impact of aerosol processes on the properties of convective systems using advanced cloud models with spectral microphysics and polarimetric radar observations.

2.1 Simulating a Mesoscale Convective System Using WRF with a New Spectral Bin Microphysics

2.1.1 Coupling of a new bin microphysics scheme with polarimetric operator

Mesoscale Convective Systems (MCSs) are an important natural phenomena that constitute an ideal framework for testing microphysical schemes in cloud-resolving models (CRM). There were four primary goals for this study: A) to develop a modified version of the spectral bin microphysics scheme implemented to WRF (referred here as FSBM-2) and to demonstrate the abilities of FSBM-2 using the well-observed MC3E-0520 squall line case as a framework; B) to establish relative role of large hail in the formation and spatial variations of mesoscale MCSs structure; C) to analyze the processes contributing to ice-particle size distributions in the convective and stratiform regions; D) to evaluate the role of aerosols in the formation of hail. The main methodology of the investigation is the comparison of results of simulations with observed data provided by polarimetric radar. Accordingly, the forward polarimetric operator (Ryzhkov et al., 2011, Snyder et al., 2015) has been implemented in the Weather Research and Forecasting Model (WRF) along with FSBM-2. FSBM-2 allows simulating hail particles with diameters up to 6 cm. The utilization of 43 mass-doubling bins allows hail up to 6 cm in diameter to be simulated. Calculations were performed for different aerosol concentrations.

In this section, we compare the results of H43 (size distributions are described using 43 bins, with maximum diameter for hail of 6 cm), H33 (size distributions are described using 33 bins, with maximum size for hail of 1.2 cm), and G33 (size distributions are described using 33 bins, with maximum size for graupel of 1.3 cm). Fig. 14 shows the fields of radar reflectivity (Ze) obtained in the observations at an altitude of 2.5 km (at 10:40 UTC) and in the three simulations (at 10:00 UTC) mentioned above. In general, the fields presented in Fig. 14 agree well with the observations for all the simulations. The

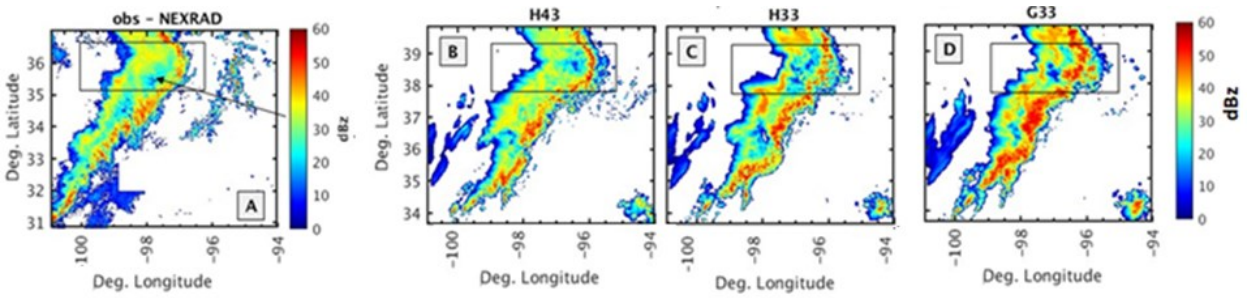

Fig. 14 The fields of radar reflectivity (Ze, in dBz) at 2.5 km altitude obtained in the observations (NEXRAD) and simulations H43, H33, and G33 at 10:00 UTC. The rectangles show the latitude band where the averaging in the north-south direction is performed (see text for details).

general structure and the alignment of the squall line spanning over ~700 km in length are captured quite well. One can see comparatively narrow lines of strong, leading convection (with Ze ranging from 45 to 55-57 dBZ in different simulations) and comparatively wide trailing stratiform areas. All simulations reproduce a unique feature seen in the observations: a transition area between the leading squall line and the trailing stratiform regions characterized by a local minimum of Ze approximately 120 km behind the convective line. Representing hail on the 33-bins mass grid (i.e., H33) leads to an increase in the width of

convective area compared to H43. These results are consistent with lower values of maximum fall speeds of hail in H33. Replacing 33-bin hail by 33-bin graupel (i.e., G33) leads to further widening of the convective area.

At 8-km altitude, a good agreement of the simulated mesoscale DCS structure with the observed one is also seen in all simulations **(**not shown, see Shpund et al, 2019**)**. The convective regions are substantially narrower than the stratiform ones. Qualitatively, H43 appears to agree with observations better than H33 and G33 as it has the narrowest area of intense convection

All simulations show a very pronounced leading convective line with relatively high Ze up to 8.0-8.5 km altitudes, in agreement with the observations. Among the simulations, H43 produces the narrowest band of enhanced Ze in the leading convection area, agreeing with the observed one the best. The lack of liquid water fraction in melting ice in the simplified description of the melting process prevents the model from simulating the bright band.

The main source of large snowflakes in the stratiform region is the diffusion growth and aggregation of ice crystals falling from the upper levels. As seen from Fig. 15**,** the concentration of ice crystals in the anvils of the deep convective clouds in and around the convective updrafts is as high as 20 cm^{-3}. These ice crystals form in convective updrafts reaching heights of ~10–12 km and are then advected both forward and backward relative to the squall line movement, forming a typical forward and trailing anvils that are known to be part of the squall-line phenomena.

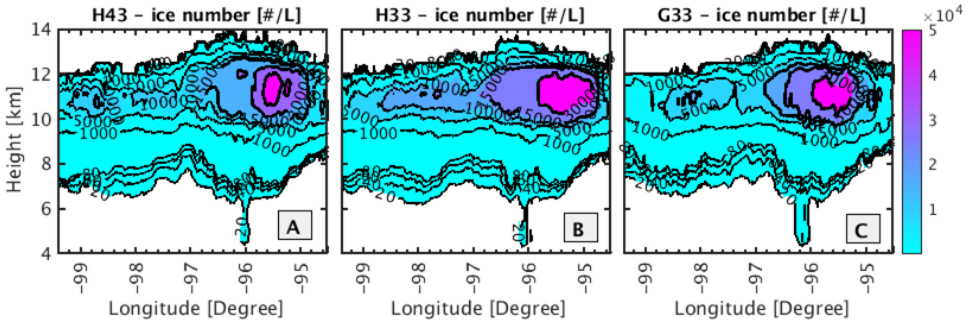

Fig. 15. Vertical cross-section of the averaged ice concentration at 10:00 UTC for H43, H33, and G33. The averaging in the north-south direction takes places within the latitude rectangle shown in Fig. 1.2, and within cloud columns where supersaturation above ice was positive and number of ice concentration was above 20 L^{-1}

Fig. 16 shows IWC (snow, in our case) mass and number distributions in the stratiform region at three different heights compared with observed data.

A comparison of rain mass distributions (RSD) at different ranges of rain rates in simulations and observations within the stratiform region is shown in Fig. 17. Thick gray circles show the averaged measurements per disdrometer station over 2 hours between 1100 and 1300 UTC, where the bars show the 10^{th} and 90^{th} percentile range. The simulated surface rain size distributions are averaged between 09:00 -10:00 UTC within the stratiform area marked by the black rectangle shown in Fig. 14. One can see a good agreement of RSDs with observations in all these simulations. However, in all simulations amount of large raindrops is underestimated. We attribute this result to the simplified parameterization of melting.

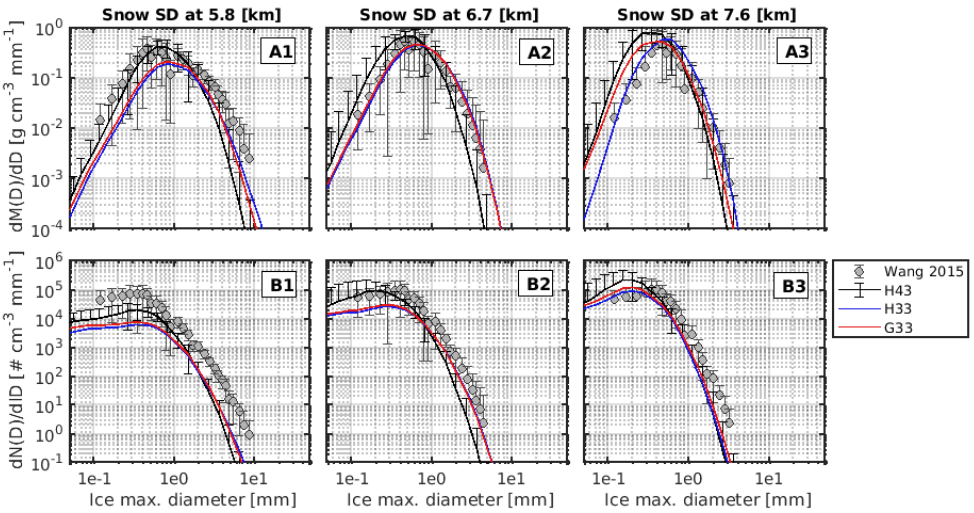

Fig. 16. Ice mass distributions (upper row) and number size distributions (bottom row) at 3 levels within the stratiform area for observation (gray circles) and simulations (H43-black, H33-blue and G33-red). The observations are from Wang et al. (2015) at 3 levels corresponding to temperatures -11ºC, -16ºC and -23ºC; The gray circles denote the 50th percentile distribution per height along 1 h from 13:54 to 14:54 UTC with the light gray bars showing the range between the 10th and 90th percentiles. For the simulations, different colors represent the 50th percentile for distributions at corresponding temperatures within +/-0.5C of the observed temperature within the stratiform region inside the rectangle shown in Fig. 1.1; the bars show the range between the 90th and 10th percentiles. Only the bars for H43 are shown, for clarity. While the mass and size distributions obtained in the observations are plotted as a function of maximum particle dimension, the simulated distributions are plotted as functions of the mass equivalent diameter.

2.1.2 Detailed melting and polarimetric signatures

As is shown in Fig. 14, a simplified approach to melting used in the first version of FSBM-2 does not allow to reproduce realistically polarimetric radar signatures below the melting level. In particular, no bright bands in the fields of radar reflectivity, Ze and no differential reflectivity Zdr were reproduced.

Taking into account the high importance of the microphysical and dynamical processes in the boundary layer, which can be observed and interpreted using the polarimetric radar signatures, a procedure for detailed melting was implemented into FSBM-2 (Shpund et al, 2020, in preparation). This procedure is described in detail in Khain and Pinsky (2018). The procedure has been implemented into HUCM and used in studies by Ryzhkov et al., 2011 and Ilotoviz et al. (2014, 2016, 2018). The detailed melting routine calculates the liquid water content (or liquid water fraction-LWF) in melting particles. If LWF in a melting particle increases up to 0.99, then this ice particle is assumed to be completely melt. The procedure implemented in FSBM-2 takes into account collisions of melting particles with all other hydrometeors and between melting particles themselves.

Fig. 18 shows the horizontal cross-section of radar reflectivity field at z=2.8 km (the level of bright band). One can see that the simplified approach does not produce bright band within the stratiform area, while the detailed melting shows clear increase in Ze.

Fig. 19 shows vertical distribution (CFAD) of radar reflectivity in H43 using a simple melting procedure (left) and detailed melting (center). One can see a good agreement with observations (right panel). A bright band is clearly seen. Besides, detailed melting leads to formation of larger raindrops (larger Ze)

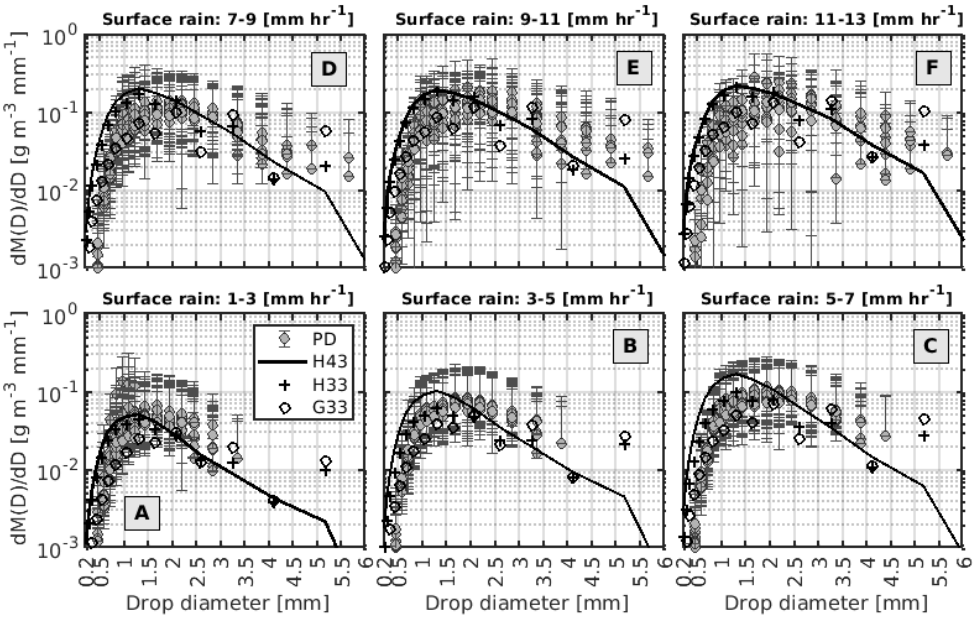

Fig. 17. Stratiform surface rain mass distribution in observations (Parsivel distrometer - PD, gray circles) and in simulations (black line – H43, black plus – H33 and black diamond – G33). For the observation, 16 PDs were used, giving rain rate and rain size distribution over 32-diameter size bins within the interval 0.06–25.2 mm (Wang et al. 2016). The gray circles represent the mean value in each size bin in each distrometer for the corresponding rain rate between 11-13 UTC. The bars correspond to 10th and 90th percentiles. For the simulation, the mean value is presented within the stratiform area defined by the rectangle in the northern part of the squall line at 9:00-10:00 UTC of the simulation with 10 min output frequency.

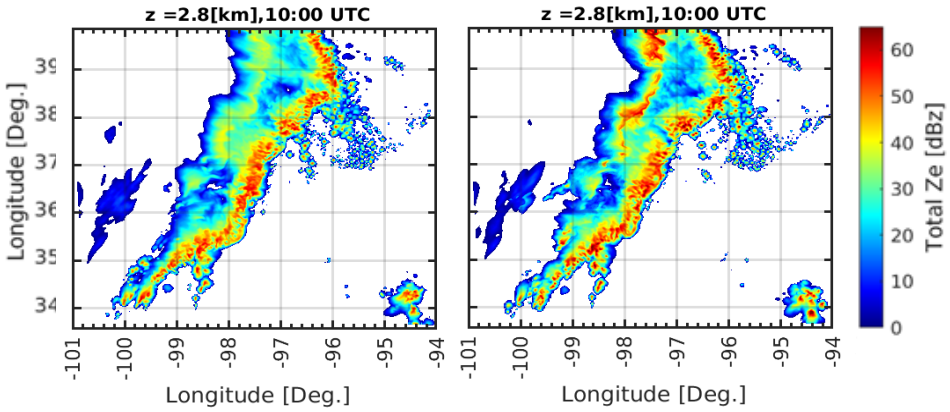

Fig. 18. Horizontal cross-sections of radar reflectivity at t=10 h in simulations of MC3E in cases of simplified melting (left) and detailed melting (right).

Fig. 20 shows the fields of Zdr in simulation with detailed melting at two height levels: 2.4 km and 2.8 km. (The simplified method does not produce Zdr). One can see that a) Zdr values are realistic; b) Zdr at 2.4 km is higher than at 2.8 km. This increase is attributed to the fact that at the bottom of melting layer the largest melting particles remain. At high values of LWF, the Zdr from these particles is close to that of

large raindrops of the same mass. It is known that large raindrops are non-spherical and produce large Zdr.

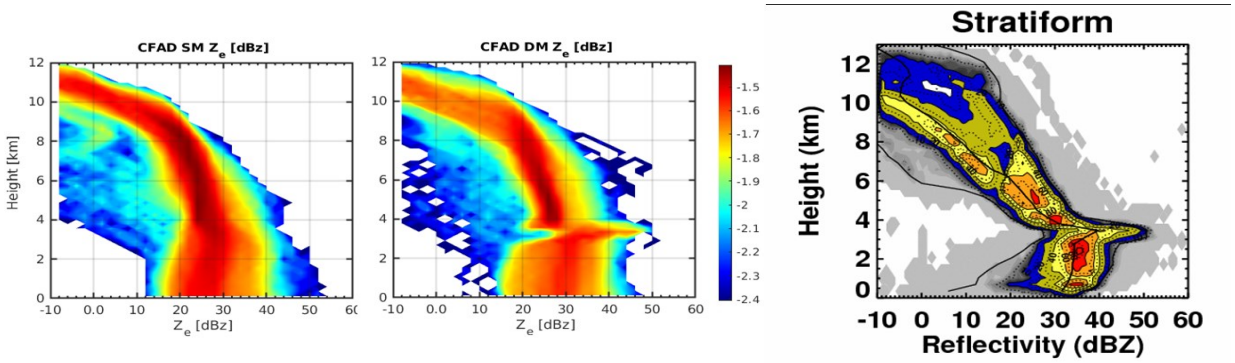

Fig. 19. Vertical distribution (CFAD) of radar reflectivity in stratiform area in H43 calculated using a simple melting procedure (left) and detailed melting (center). One can see a good agreement with observations (right panel).

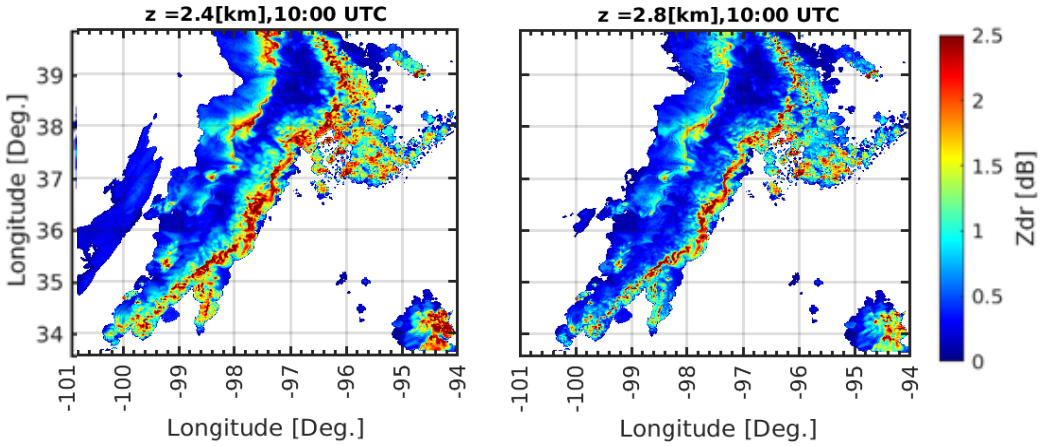

Fig. 20. Fields of Zdr in the simulation H43 with detailed melting at two height levels: 2.4 km and 2.8 km at t=10 h UTC.

2.1.3 Conclusions

The mesoscale DCS from the Midlatitude Continental Convective Clouds Experiment that occurred on 19–20 May, 2011 (MC3E-0520), was simulated using a new version of the Fast SBM microphysics scheme embedded into WRF (FSBM-2). Utilization of the 43-bins version allows larger particles such as hailstones of up to 6 cm in diameter to be simulated. The new scheme includes a forward polarimetric radar operator allowing explicit calculation of polarimetric radar signatures. Lastly, the novel procedure of detailed melting was implemented.

The main results of the study can be summarized as follows.

a) FSBM-2 produces a general structure of the MC3E-0520 realistically. The simulated MCS have geometric similarity with the observed system, realistic Ze at different altitudes, and realistic area ratios between convective and stratiform regions.

b) It is important to take into account the existence of large hail particles in the convective updrafts.

c) FSBM-2 realistically simulates ice mass distributions in the stratiform region. Rain drop size distributions simulated by FSBM-2 are also in good agreement with observations.

d) New detailed melting and the forward polarimetric operator allow reproducing well observed polarimetric signatures of the MC3E.

2.2 Effects of sea spray on microphysics and dynamics of tropical cyclones

2.2.1 Objectives

An important component of the TC-ocean interaction is sea spray generation within the surface layer at strong winds. A wide spectrum of sea spray particles (SSP) is generated during wave-breaking events - the size range of sea-spray droplets can range from ~0.01 μm to ~600 μm The concentration of the SSP can exceed several hundreds cm^{-3} . TC simulations using different cloud resolving models with spectral bin microphysics have demonstrated that TC intensity is highly sensitive to aerosols (e.g. Khain et al. 2016; Lynn et al. 2016; Qu et al. 2017). It has been shown that aerosols serving as cloud condensational nuclei (CCN) intensify the TC if the CCN penetrate the clouds at the center of the TC but weaken it if they penetrate the clouds at the TC periphery. The *effects of SSP with realistically wide size distribution on microphysical structure and intensity of tropical cyclones were not considered in literature*.

The SSP concentration and SSP size distribution width increases with the maximum surface wind speed. Therefore, SSP concentration should be highest at the radii of maximum winds, i.e., in the eyewall zone. We hypothesized that SSP would be an important component in shaping the microphysical structure and dynamics of deep convective clouds in the eyewall of TCs, changes which may affect the intensity of TCs themselves. Evidence of the microphysical effect that SSP might have on a TC's eyewall clouds was provided by satellite measurements of the effective drop radius on tops of growing clouds in more than 20 TCs. For example, satellite measurements from the Aqua and Terra satellites made at cloud tops in the eyewalls of Hurricanes Epsilon (2005) and Frances (2004) showed r_{eff} of ~17 μm and ~13 μm at the altitude corresponding to 10^0C at maximum winds of ~33 $m\ s^{-1}$ and ~50 $m\ s^{-1}$, respectively. These values are typical for polluted continental clouds and are much lower than those observed in maritime convective clouds outside of the eyewalls (~25 μm). The effective radius was found to decrease with increasing surface wind speeds. Shpund et al. (2019b) (hereafter, SKR) studied the effects of SSP on the microphysics and dynamics of single deep convective clouds under conditions typical of the eyewalls of hurricanes using a parcel model as well as the Hebrew University Cloud Model (HUCM), both with bin microphysics. It was shown that sea spray leads to a dramatic increase in droplet concentration and a corresponding decrease in r_{eff} . It was also shown that SSP lead to an increase in the rates of all microphysical processes, to an increase in cloud water content and cloud ice content, as well to an increase in maximum updrafts and in cloud top height. In Shpund et al (2019c) we described the role of suspended SSP in shaping the microphysical structure and intensity of an idealized TC. This study is described in more detail below.

2.2.2 Model Description and simulation design

The effects of SSP on the vertical cloud microstructure as well as on the intensity of an idealized TC were investigated in simulations where WRF model with bin microphysics (FSBM-2) was coupled with the Lagrangian- Eulerian model of the hurricane boundary layer (LEM). The FSBM-2 was described in the previous section (see Shpund et al, 2019a). The design of simulations was as follows. The idealized TC numerical experiments are conducted using the WRF (version 3.8.1). All the simulations use 55 vertical levels stretching logarithmically from the ocean surface at 1015 hPa up to the model top of 20 km. A triple-nested mesh is used with horizontal grid spacing of 9 km (outer grid), 3 km (middle grid), and 1 km (inner grid); the respective numbers of domain grid points are 480 x 480, 481 x 481, and 720 x 720. The innermost domain is large enough (720 km) to describe both the vortex inner core and the outer rainbands. The inner-nested grids are located at the center of their parent domains, and a vortex-following technique is used to allow for long time integration. The TC development was triggered by an initial Rankine vortex with maximum tangential wind of 15 ms^{-1} at the radius of 135 km. Fast Spectral Bin Microphysics (FSBM-2) scheme was used to calculate cloud microphysical processes in all three domains.

To calculate radar characteristics, a polarimetric forward operator was used (Ryzhkov et al. 2011; Snyder et al. 2015). The operator allows to calculate all main radar characteristics that can be measured by a dual-polarization radar network (e.g., WSR-88D in the United States). In the simulation without SSP (hereafter: *NoSpray*), the background size distribution of dry CCN typical of maritime atmosphere was used following Ghan et al. (2011). The size distribution of CCN is defined on a grid containing 33 mass-doubling bins with a maximum dry CCN radius of 2 μm. The initial CCN size distribution is given as the sum of three log-normal distributions representing the smallest CCN (Aitken mode, centered at 0.005 μm), medium-sized CCN (accumulation mode, centered at 0.035 μm) and largest CCN (coarse mode, centered at 0.31 μm) (Fig. 21). The corresponding CCN concentrations in the modes are of 170 cm^{-3}, 30 cm^{-3} and 1.5 cm^{-3}. The total CCN concentration was, therefore, around 200 cm^{-3}, while the fraction of CCN with radii exceeding 0.01 μm was about 30 cm^{-3}.

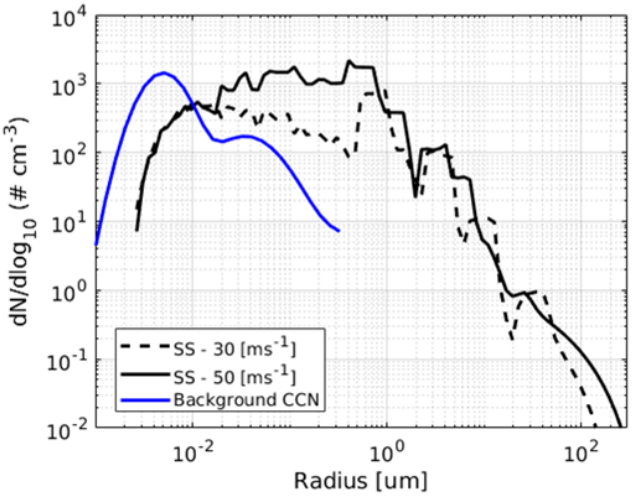

Fig. 21. Size distributions of SSP and background CCN used in simulations of TC. Blue line: initial background CCN size distribution for background maritime conditions; black lines: horizontally averaged equilibrium SSP simulated using LEM, taken at the level z=350 m at U_{10}=30 $m\ s^{-1}$ (black dashed line) and U_{10}= 50 $m\ s^{-1}$ (black solid line).

In the simulation with SSP (hereafter: *Spray*), SSP size distributions obtained in separate off-line LEM simulations (Shpund et al., 2014 and 2019a (hereafter, SKR)) were added to the background CCN distribution within a layer of 600 m in depth. The LEM is a slab-symmetric model with a computational area assumed to be perpendicular to the background TC wind. This configuration allows us to describe in detail the vertical transport of SSP by roll vortices elongated

along the background wind. The LEM computational area is covered with 3750 interacting adjacent Lagrangian air parcels with a characteristic linear size of ~8 m, which is indicative of the high spatial resolution of the simulations. These parcels move within a turbulent-like flow field generated by a turbulent model in line with the observed data. The microphysics of each Lagrangian cloud parcel includes the diffusional growth/evaporation equation used for wetted aerosols and water drops as well as the equation for supersaturation and the stochastic collision equation describing collisions between drops. The droplet size distribution of both non-activated aerosol particles and cloud drops is calculated on a mass grid containing 500 bins within a radius range of 0.005 μm to 2000 μm. The high salinity of SSP enables them to grow at relative humidity RH ~95%, which in turn affects their thermodynamic behavior. The SSP fluxes and size distributions on the surface depend on the background wind U_{10} at z=10 m. The SSP source functions (with radii ranging from ~0.01 μm to ~ 600 μm) at different U_{10} were determined by combining observed size distributions measured in real storms and those measured under laboratory conditions. An example of the "equilibrium" SSP size distributions simulated using the LEM at U_{10}=30 $m\ s^{-1}$ and 50 $m\ s^{-1}$ at z=350 m is shown in Fig. 21 (black lines). The size distributions shown in Fig. 2.1 are obtained when approximate quasi-equilibrium state was reached. In *Spray*, in grid points where U_{10} exceeded 20 ms^{-1}, the SSP size distributions corresponding to the values of U_{10} were implemented within the lower 600 m depth layer. The equilibrium SSP distributions were updated at all grid points below cloud base at every dynamical time step depending on the U_{10} wind speed.

2.2.3. The effects of sea-spray on idealized TC

Fig. 22 shows vertical cross section through the TC center in the fields of droplet effective radius at t=48h in *NoSpray* and *Spray*. One can see that, in *NoSpray*, the microphysical structure of clouds in the eyewall is typical of extreme maritime clouds (high r_eff). In *Spray*, the microphysical structure of clouds in the eyewall dramatically differs from that of clouds outside of it.

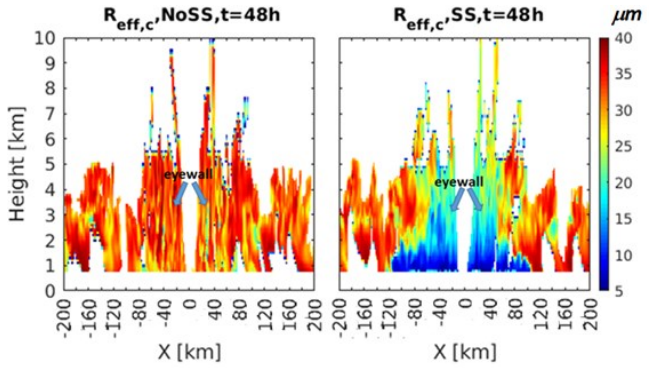

Fig. 22. Vertical cross section through the TC center in the fields of droplet effective radius at t=48h. Left: *NoSpray*; right: *Spray*.

The low r_{eff} values are determined by two main factors: (a) high concentration of small droplets being advected upward and (b) in-cloud nucleation of new droplets from the smallest CCN. As was mentioned above, the SSP distribution contains a significant amount of very small SSP which are activated at higher levels, where supersaturation increases due to an increase in W and a decrease in droplet concentration by accretion. One can see that r_{eff} decreases toward areas of maximum SSP concentration, i.e., toward the regions of stronger winds in agreement with observations. The effect of SSP is not limited to warm microphysics but inevitably leads to changes in ice microphysics as well. The mass contents of snow and graupel are larger in *Spray* due to the more intense accretion of small droplets

at high levels. The results obtained show that SSP increase liquid and ice contents, as well as the cloud top height of the eyewall clouds with corresponding increase in radar reflectivity which becomes close to the observations by Heymsfield et al. (2010). Fig. 23 shows that the TC in the *Spray* is more intense, and the difference in the intensities increases after 22-24h. The minimum pressure shows continuing deepening, as the radial gradients are larger in *Spray* throughout the simulation. The difference between the maximum wind speeds in the simulations exceeds 10 ms^{-1}.

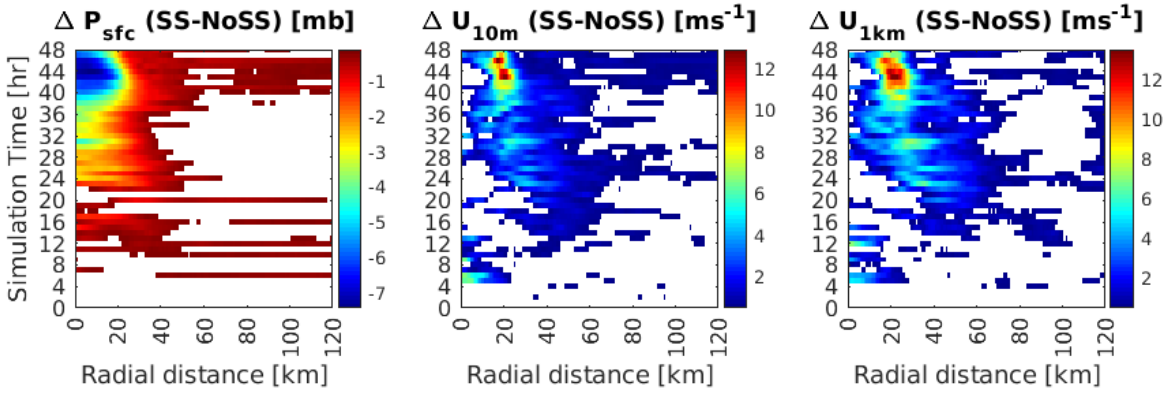

Fig. 23. Radial-time dependencies of *Spray* - *NoSpray* differences between the azimuthally averaged fields of surface pressure (left), as well as between the azimuthally averaged fields of wind speed at 10 m height (middle) and at 1 km height (right).

2.2.4. Discussion and conclusions

This is the first study of the sea-spray microphysical effects on microphysical and dynamical structures of an idealized TC by means of cloud-resolving simulations using WRF with spectral bin microphysics. It is shown that, in the SSP-affected eyewall, clouds have unique properties combining both continental and maritime features. These clouds contain raindrops already at cloud base since the largest SSP are small raindrops that are intensively collecting smaller droplets. This feature is "more maritime" than of extreme maritime clouds. At the same time, the droplet number concentration in the eyewall clouds is as high as 500-700 cm^{-3} below the freezing level and remains significant above this level. Such concentrations are typical of polluted continental clouds. As a result, the distributions of cloud droplets in the eyewall clouds have very low effective radii, not exceeding 15-17 μm until high altitudes. The formation of such small values of the effective radius was observed from satellites. The increase in the drop number concentration and CWC in *Spray* foster larger amounts of snow, graupel and ice at high levels. These unique properties of eyewall clouds affected by SSP allow us to explain observed features like high ice crystal concentrations in cloud anvils, intense lightning and a low droplet effective radius - despite the considerable rainfall. In agreement with observations, the radar reflectivity in the eyewall becomes substantially higher than that in deep convective clouds in the tropics under low wind conditions. The comparison of the results of TC simulations with and without SSP taken into account clearly shows that SSP lead to an intensification of TC. We have shown that incorporating wind-generated SSP increases TC intensity by invigorating the inner convective cloud bands as a result of the SSP impacts on cloud microphysical processes. The increase in the SSP production with the increase in

wind speed *constitutes a positive feedback loop that supports intensification of the TC*. Thus, the SSP effects is a plausible mechanism fostering fast storm development.

2.3. Relationship between aerosols, hail microphysics, and Z_{DR} columns in convective storms

2.3.1 Objectives and method of investigation

The goals of the investigation were: a) To clarify the mechanisms of formation of big hail; b) To establish the role of aerosols in formation of big hail; c) To clarify the mechanism of formation of Zdr columns; d) To find relationship between the height of Zdr column, hail size and the aerosol concentration.

In order to address the objectives, a new version of the Hebrew University Cloud Model (HUCM) with spectral bin microphysics has been developed. In order to describe properly hail formation, the ice microphysics of HUCM was substantially modified: a) The number of bins describing size hydrometeor size distributions was increased to 43. This allows to describe hailstones with diameters up to 6 cm; b) Spontaneous breakup of large drops was implemented; c) In order to take into account the fact that freezing of raindrops is not instantaneous, but may require significant (up to a few minutes) time, a new hydrometeor type called "freezing drops" (FD) was implemented. The rate of liquid water freezing was calculated following Phillips et al. (2015). As a result, liquid water fraction was calculated at T<0 C in each particle belonging to FD, graupel and hail' d) The description of hail growth was substantially modified. Two regimes of hail growth were considered: dry growth, if the particle surface is dry and wet growth, when particle is covered by the liquid water shell. The liquid shell arises in the case of intense riming by collection of multiple cloud droplets, so that released latent heat does not allow all water to freeze; e) Connect the type of hail growth with the value of differential reflectivity, the aspect ratio of hail growing by wet growth was calculated to obey polarimetric observations.

Note that Zdr from hail growing by dry growth is close to 0 dB because its shape is close to spherical and because of hailstones rotation during their fall. At the same time, hail growing by wet growth has a significant Zdr because of liquid shell that creates water band near particle equator. A mid-latitude summertime hail storm with hailstones up to several cm in diameter was simulated for several aerosol concentrations. A polarimetric radar forward operator was used to calculate radar reflectivity and differential reflectivity Z_{DR}.

2.3.2. Formation of Z_{DR} columns and hail in the case of high CCN concentration

Fig. 24 shows the field of radar reflectivity Z_H and the Z_{DR} fields, as well as hydrometeor mass distributions within in the updraft, during the mature stage of the storm evolution. The maximum Z_H exceeds 65 dBZ and is attributed to hail. Strong updraft transports hail upward, so Z_H remains high (e.g., exceeding 50 dBZ) up to ~ 10 km height. This is a typical feature of hailstorms. One can see a pronounced Z_{DR} column with top height exceeding 6 km. The microphysical composition of hydrometeors comprising the Z_H and Z_{DR} fields is shown in the left column, where the mass distributions of different hydrometeors at several altitudes within the updraft are presented. Mass distributions of liquid drops indicate the presence of raindrops as well as a significant mass of cloud droplets (i.e., high CWC) with a peak at droplet diameter of ~20 μm. The high concentration of small cloud droplets is caused by the high aerosol concentration. One can see that hail particles exist in the updraft at elevations as low as 3 km, where temperatures are greater than 0°C. These hail particles entered the cloud updrafts in the

convergence zone in the lower part of the deep convective cloud. Since the onset of freezing results in the conversion of raindrops to freezing drops (FDs), the concentration of rain decreases with height in the updraft. Complete freezing of FDs and accretion of small droplets lead to an increase in hail mass and hail size with height in the updraft. The largest raindrops near the surface produce Z_{DR} of about 3 dB. Maximum Z_{DR} above the freezing level at the considered time (78 min) is about 3.5 dB and is reached at ~1 km above freezing level. Since Z_{DR} from dry hail is less than 1 dB, a higher value of Z_{DR} is caused by hail containing liquid water and growing in the wet growth regime. Indeed, as can be seen from hail size distributions in the right panels of Fig. 24, hail particles of the majority of sizes grow in the wet growth regime, i.e., they are covered by a film of liquid water. Even at an altitude of 6.5 km, hailstones with diameters exceeding 1 cm continue growing in the wet growth regime.

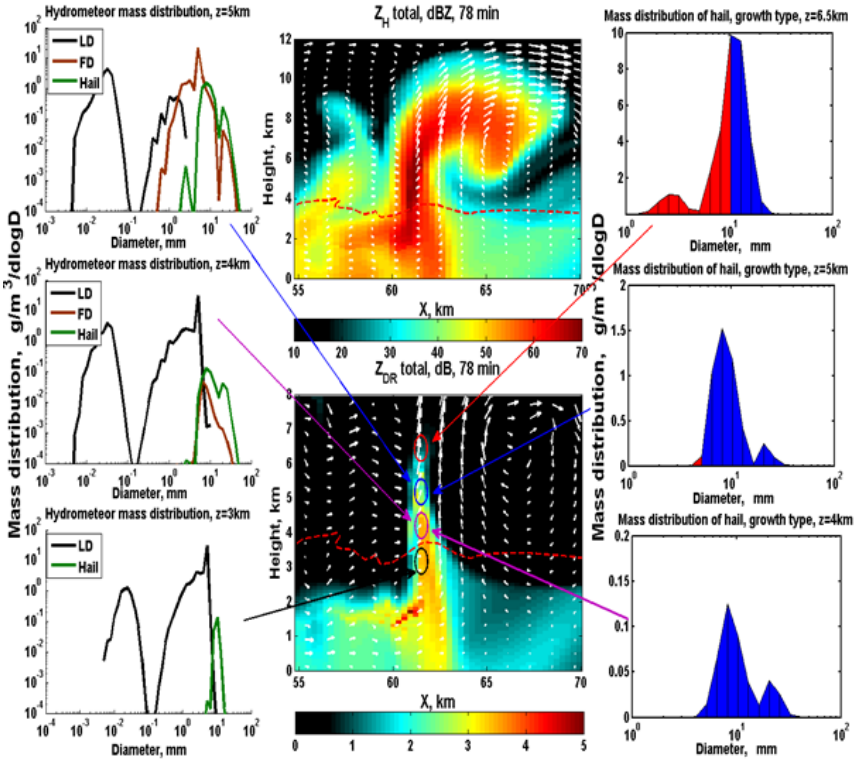

Fig. 24. Middle: The field of Z_H and Z_{DR} (colored shading; dBZ and dB) in a mature storm in the simulation with high CCN concentration. The white arrows indicate wind velocities. Ellipses show locations at which particle mass distributions are plotted (x = 61.5km). Red dashed line shows the 0°C isotherm. The left column shows the mass distributions in cloud updraft at heights of 3 km, 4 km, and 5 km showing liquid drops (LD) (black curves), hail (green), and freezing drops (brown). The right column contains hail mass distributions at three altitudes. The parts of hail size distributions marked blue corresponds to the wet growth regime; the part of mass distribution of hail particles growing in dry growth regime is marked red.

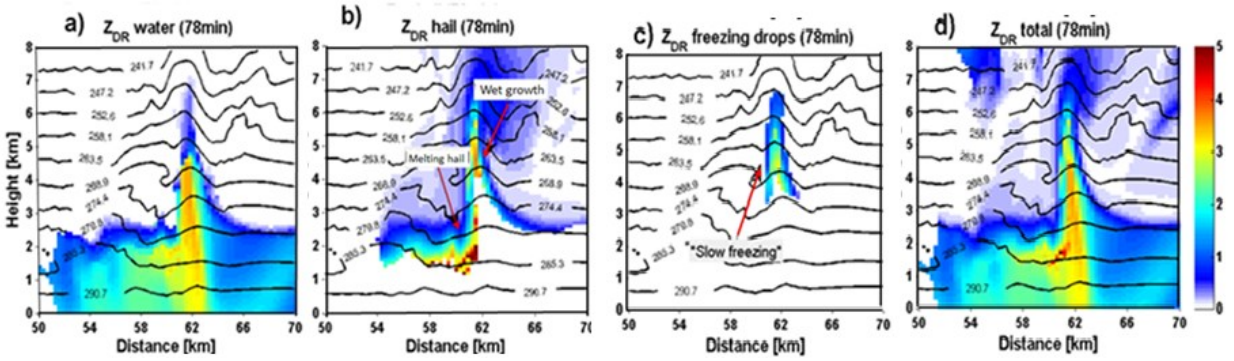

Fig. 25. Fields of Z_{DR} produced by (a) liquid drops, (b) hail, and (c) freezing drops at 78 min. Total (or net) Z_{DR} is shown in panel (d). Temperature contours are plotted with increments of 5.5 K, starting at 290.7 K near the ground. Red arrows show zones of wet growth of hail, and of slow freezing of liquid in freezing drops. The threshold for calculating a Z_{DR} for hail is 0.01 $g\ m^{-3}$

Fig. 25 presents the Z_{DR} fields produced by each hydrometeor type separately. Z_{DR} from water is substantial from the ground up to 4.8 km where T~-6.5℃ (Fig. 25a). The Z_{DR} produced by hail increases in the upper portion on the Z_{DR} column up to ~6.5 km (T~-18.5℃). In addition, increased Z_{DR} is found at the edge of cloud, where falling hail collects droplets, as well as in the narrow layer below the melting level. FDs produce moderate Z_{DR} (e.g., 2–3 dB) within a comparatively wide layer from 4 to 6.5 km (T between -2℃ up to -18.5℃). This significant thickness of the layer where FDs exist and contribute to Z_{DR} can be attributed to intense accretion of supercooled liquid droplets (Fig. 25c). The "net" Z_{DR} that results from the contributions of all hydrometeor species clearly shows the Z_{DR} column extending to an altitude of 6.5 km where T~-18.5℃ (Fig. 25d). Hail reaches the surface periodically for small periods of time. Hail reaches the surface periodically for short periods of time.

2.3.3. Formation of Z_{DR} columns and hail in the case of low CCN concentration

Fig. 26 shows the fields of Z_H and Z_{DR}, as well as hydrometeor mass distributions within the updraft at the mature stage of the storm in the low CCN concentration case. Note first that the maximum of Z_H is about 55 dBZ, which is 10 dBZ lower than in the high CCN case (Fig. 24). The lower reflectivity is the result of the smaller sizes of hydrometeors in the clean case. The values of Z_H rapidly decrease above 8 km in the clean case, whereas they extended to ~10 km height in the polluted case. In contrast to the polluted case, the maximum of Z_H occurs below the freezing layer. This reflectivity maximum is mostly associated with raindrops, while the reflectivity maximum is primrily associated with hail in the polluted case. There is no pronounced Z_{DR} column in the clean case: a zone of enhanced Z_{DR} only slightly extends above the 0°C isotherm.

The mass distributions of different hydrometeor types are plotted (left panels in Fig. 26) at altitudes of 3 km, 4 km, and 5 km in the maximum updraft. The mass distributions of liquid drops (black curves) do not contain small (e.g., 20 μm) cloud droplets, which dramatically differs from the polluted case. The concentration of the largest raindrops rapidly decreases with height due to freezing because of the higher probability of larger raindrops to freeze. Owing to the lack of supercooled droplets (CWC is ~1 $g\ m^{-3}$ at 4km in the clean case, while in polluted case the CWC is twice as large at the same altitude), the accretion rate is comparatively low, so FDs rapidly freeze to produce hail with sizes that do not exceed 1.3 cm in

diameter. This hail is substantially smaller than in the polluted case where D reached 4–5 cm. The size of freezing drops is also smaller in this clean case. The mass distributions of FDs and hail at two height levels showing the type of growth regimes are presented in the right column of Fig. 26. Freezing drops and hail grow in the wet growth regime only in the vicinity of the 0°C isotherm. At altitude of 5 km, hail particles of all sizes grow in dry growth regime due to the lack of supercooled water. Since Z_{DR} values produced by dry hail and remaining small raindrops are low, Z_{DR} is also low above 4 km. In agreement with growth regimes shown in Fig. 26, non-zero LWF in FDs is found only within the 3.3–4.5 km layer. Non-zero LWF in hail occurs within a narrow (500 m depth) layer just below the freezing level, where small hail particles melt.

Fig. 27 shows Z_{DR} fields produced by hydrometeors of different types. We see again that, at low CCN concentration, a robust Z_{DR} column (above freezing level) does not form. The largest Z_{DR} values produced by raindrops are not located in the updraft but in the zone of hail fall and melting (Fig. 27a). FDs rapidly freeze completely, so there are only a few FDs above 5 km (Fig. 27c). Since hail (Fig. 27b) grows in the wet regime near the freezing level, the Z_{DR} values (Fig. 27d) are substantially lower than in the polluted case.

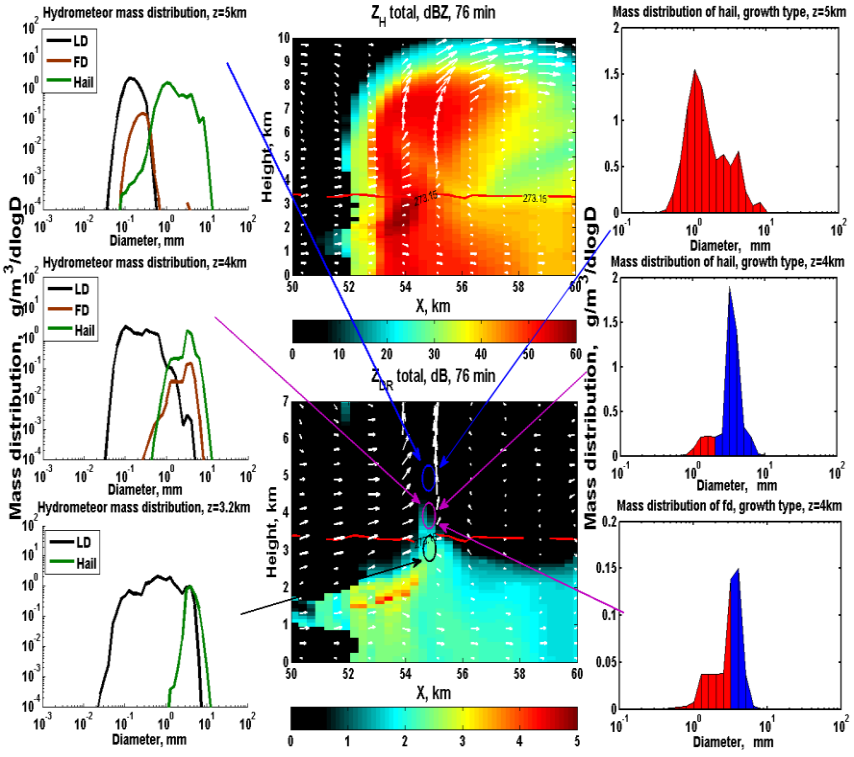

Fig. 26. The same as in Fig. 24, but for low CCN concentration.

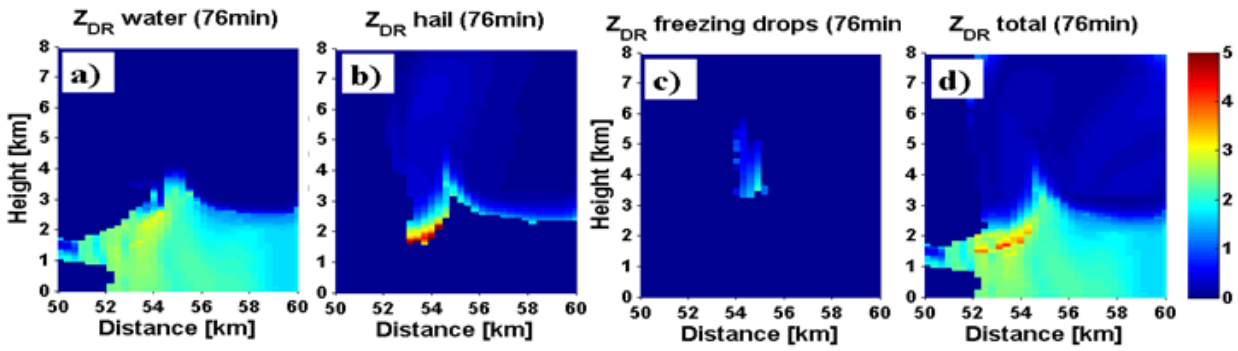

Fig. 27. The same as in Fig. 25 , but for low CCN concentration.

2.3.4 Relationships between Z_{DR}, vertical velocity, and hail parameters

Fig. 28 presents scatterplots showing the relationship between the maximum height of (a) 1 dB and (b) 2 dB contour of Z_{DR} (above local 0°C level) and the vertical velocity calculated at these heights under different aerosol concentrations. In all cases, correlations are high. The lower CCN cases generally had smaller Z_{DR} columns, but they also generally had weaker updrafts; the higher CCN cases had larger Z_{DR} columns and strong updrafts. The results indicate that Z_{DR} columns can be likely used for evaluating vertical velocity and even vertical velocity profiles in deep convective clouds.

Fig. 29 shows scatterplots of maximum values of Z_{DR} above the 0°C level versus maximum hail mass and hail mean volume radius near the surface. The correlations were calculated only for polluted cases (1000-3000 cm^{-3}) because of the lack of sufficient statistics in rare cases when hail reaches the surface in clean cases. The increase in height and volume of a Z_{DR} column can be a good predictor of a prominent hail shaft. Taking into account that the height and volume of Z_{DR} columns increase with aerosol concentration, one can see clear dependence of the total mass and size of hail on aerosols.

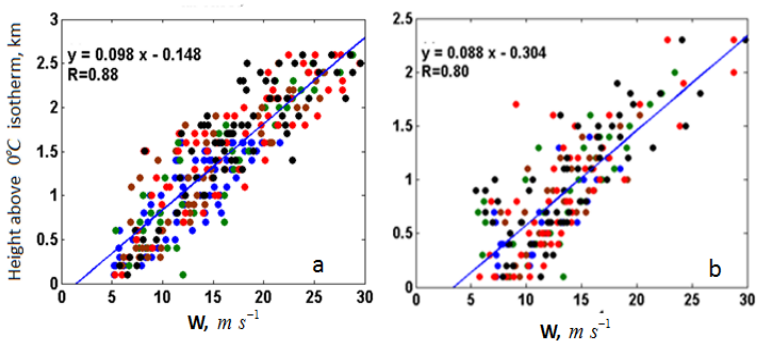

Fig. 28. (a) Scatterplot of the height of Z_{DR} = 1 dB vs. vertical velocity at these heights for different aerosols concentrations. (b) Similar to (a) but for Z_{DR} = 2 dB. Different concentrations of CCN are marked by different colors: blue - 100cm^{-3}; green - 400cm^{-3}; brown -1000 cm^{-3}; red – 2000 cm^{-3} and black - 3000cm^{-3}.

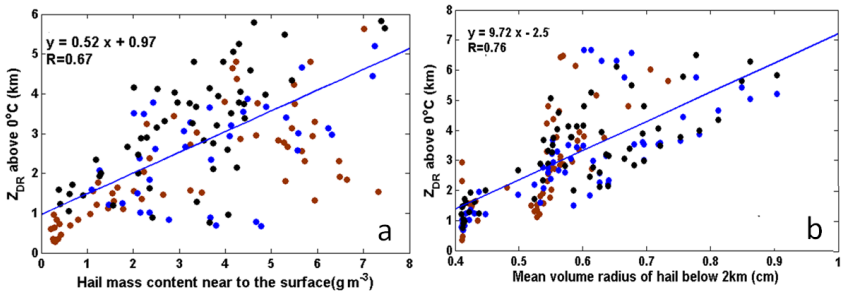

Fig. 29. Scatterplots showing the correlation between the maximal Z_{DR} values above the 0°C level and (a) maximum of hail mass content near the surface (below 1 km) and (b) mean volume radius of hail particles under different aerosols concentrations: brown - 1000 cm^{-3}, blue -2000 cm^{-3}, and black - 3000 cm^{-3}.

2.3.5 Conclusions

The results show that Z_{DR} columns are associated with raindrops and with hail particles growing in a wet growth regime within convective updrafts. The height and volume of Z_{DR} columns increases with an increase in aerosol concentration. Small hail forming under clean conditions grows in updrafts largely in a dry growth regime corresponding to low Z_{DR}. Characteristics of Z_{DR} columns are highly correlated with vertical velocity, hail size and aerosol concentration.

2.4. Turbulent mixing

Significant efforts were made to investigate the physics of turbulent mixing and effects of mixing on the formation microstructure and dynamics of non-precipitating clouds. The studies can be separated in two groups: a) in studies by Pinsky et al., (2016a,b, 2018); Pinsky and Khain, (2018) mixing between two volumes within one adiabatic volume is considered and the evolution of droplet size distributions in the course of mixing is considered. The transition to the final equilibrium is simulated. It is shown that mixing leads to broadening of the droplet size distributions. The new evaporation-diffusion equation is derived and used for the analysis. B) In studies by Magaritz-Ronen et al, (2016) ; Khain et al.(2018) and Pinsky and Khain (2018, 2019 a-c) interaction of clouds with their environment is considered (instead of mixing of two volumes within one mixing volumes). As a result, we investigated non-stationary problem that has no equilibrium final solution. It is shown that a transition zone arises between clouds and their environment characterized by rapid decrease in liquid water content and droplet concentration. Effective radius remains nearly unchanged within a significant fraction of the transition zone. The formation of humid shell and its width are evaluated.

III. Examining multifrequency polarimetric ARM radar data to improve microphysical parametrizations in the models, develop new radar retrieval methodologies, and validate their efficiency.

Multiparameter radar measurements utilizing novel retrieval methodologies have been used in a number of field campaigns in different parts of the world including continental US (e.g.,

Oklahoma), Northern Slope of Alaska, and Europe. Herein, we summarize four such observational studies with results summarized in published journal articles.

3.1 Midlatitude Continental Convective Clouds Experiment (MC3E)

The polarimetric radar retrievals of DSD in rain and the most advanced radar technique for rainfall estimation based on the use of specific attenuation have been utilized to validate the NASA NU-WRF model simulations of the MCS observed on 20 May 2011 (Fridlind et al. 2017). General conclusion from the study is that the NU-WRF model tends to overestimate the median size of ice particles and raindrops and underestimate their total number concentration. This is demonstrated via comparison with the in situ aircraft measurements and radar retrievals of the mean volume diameter of raindrops D_m estimated from differential reflectivity Z_{DR}.

A novel radar technique for matching the results of polarimetric microphysical retrievals with in situ aircraft measurements has been developed and described in the MS thesis of A. Murphy and a journal article (Murphy et al. 2019). It is based on the use of the vertical profiles of polarimetric radar variables and retrieved IWC, D_m, and N_t in a column moving with an aircraft to insure collocation of radar data with in situ aircraft measurements. This implies the use of a special technique for processing and displaying polarimetric radar data – Columnar Vertical Profiles (CVP). This technique was first tested for the MCS on 20 May 2011. The temporal evolution of CVP moving with the aircraft is illustrated in Fig. 30.

Temporal dependencies of the radar-retrieved IWC, D_m, and N_t along the aircraft track are displayed in Fig. 31. The retrieved microphysical parameters of ice are in good agreement with their direct measurements onboard an aircraft (Murphy et al. 2019). The best agreement between the retrieved microphysical parameters (dots) and in situ measurements (solid curves) is achieved for the mean volume diameter D_m and ice water content IWC in the dendritic growth layer in the temperature interval between -10 and -20ºC. The initial validation results are promising and call for more comprehensive and systematic studies.

3.2. Multisensor characterization of the MCS anvils.

The anvils of MCS, tropical cyclones, and MCS extend over large areas and play very important role in the radiative balance of atmosphere. Polarimetric radar signatures in anvils were in a focus of our studies during the project. One of the interesting features observed in the MCS anvils in the US (Oklahoma) and Europe (Germany) was an enhancement of differential reflectivity Z_{DR} (and sometimes K_{DP}) near the bottom of anvil (see Fig. 32b). This signature is often observed along the mammatus-bearing anvil bases. The value of Z_{DR} within mammatus exceeds 2 dB in the so-called Pentecost storm in Germany and in several Oklahoma severe convective storms examined in the study by Troemel et al. (2017). Observations from a zenith-pointing Ka-band cloud radar and a Doppler wind lidar during the Pentecost storm indicate the presence of a supercooled liquid layer of at least 200 – 300-m depth near the anvil base at

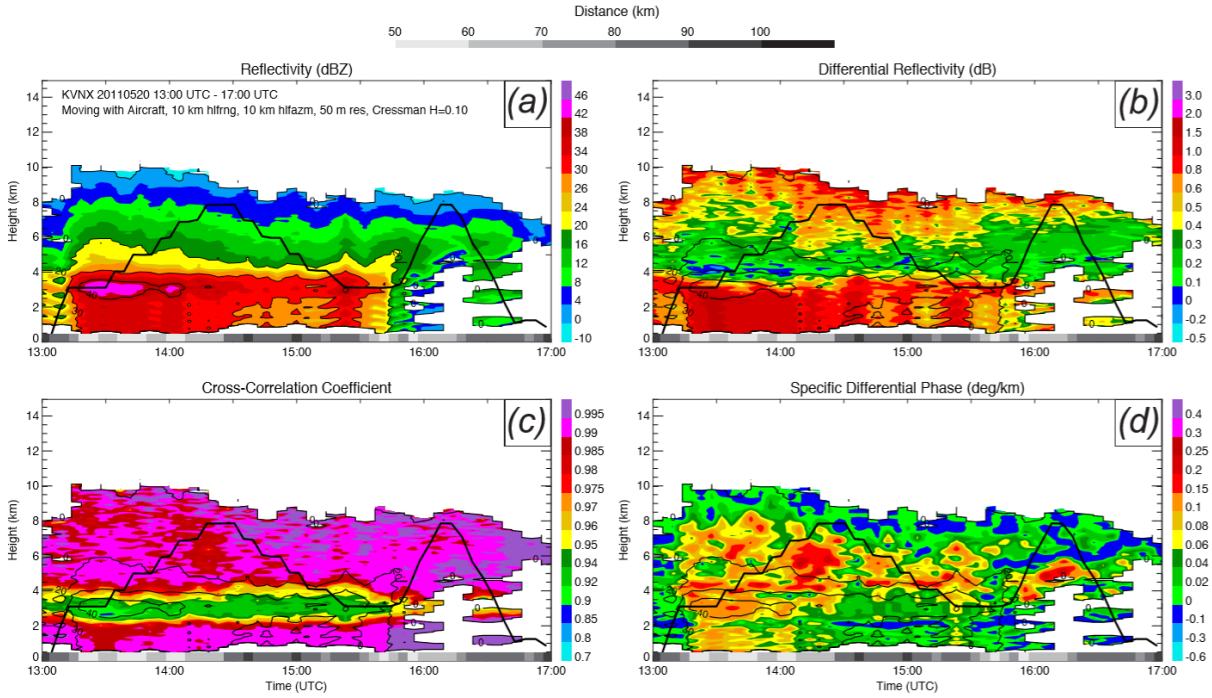

Fig. 30. Moving CVP using data from the KVNX WSR-88D radar on May 20, 2011 from 13 – 17 UTC. The CVP column moved with the location of the research aircraft flying during the MC3E campaign. The black line overlaid on each panel represents the altitude of the aircraft with time. Vertical data spacing in the CVP is 50 m, and the column base size is 20 km in range and 20° in azimuth. Distance from the radar for each scan is denoted by different shades of grey just above the x-axis on each panel. From Murphy et al. (2019).

temperatures between -15 and -30ºC (Fig. 32c,d). These liquid drops, which are presumably generated in localized areas of vertical velocities up to 1.5 m s^{-1}, coexist with ice particles identified by cloud radar. It is hypothesized that pristine crystals grow rapidly within these layers of supercooled water, and that oriented planar ice crystals falling from the liquid layers lead to high Z_{DR}.

3.3 The synergy between cloud radar polarimetry and Doppler spectral analysis in deep cold precipitating systems in the Arctic

The synergy between radar polarimetry and Doppler spectral analysis from vertically pointing cloud radars was explored in the study of Oue et al. (2018). Data were collected by the ARM Mobile Facility at the Oliktok, Alaska site instrumented with a Ka-band ARM Zenith pointing Radar (KAZR) and Ka/W-band Scanning ARM Cloud Radars (Ka/W-SACR2) with polarimetric capability. Arctic ice and mixed-phase clouds characterized by a variety of ice particle types were in a focus of this study. The results illustrate the frequent occurrence of multimodal Doppler spectra in the dendritic growth layer (DGL) where a quasi-spherical ice seeding from aloft was mixed with a locally generated very anisotropic ice (Fig. 33). The ice

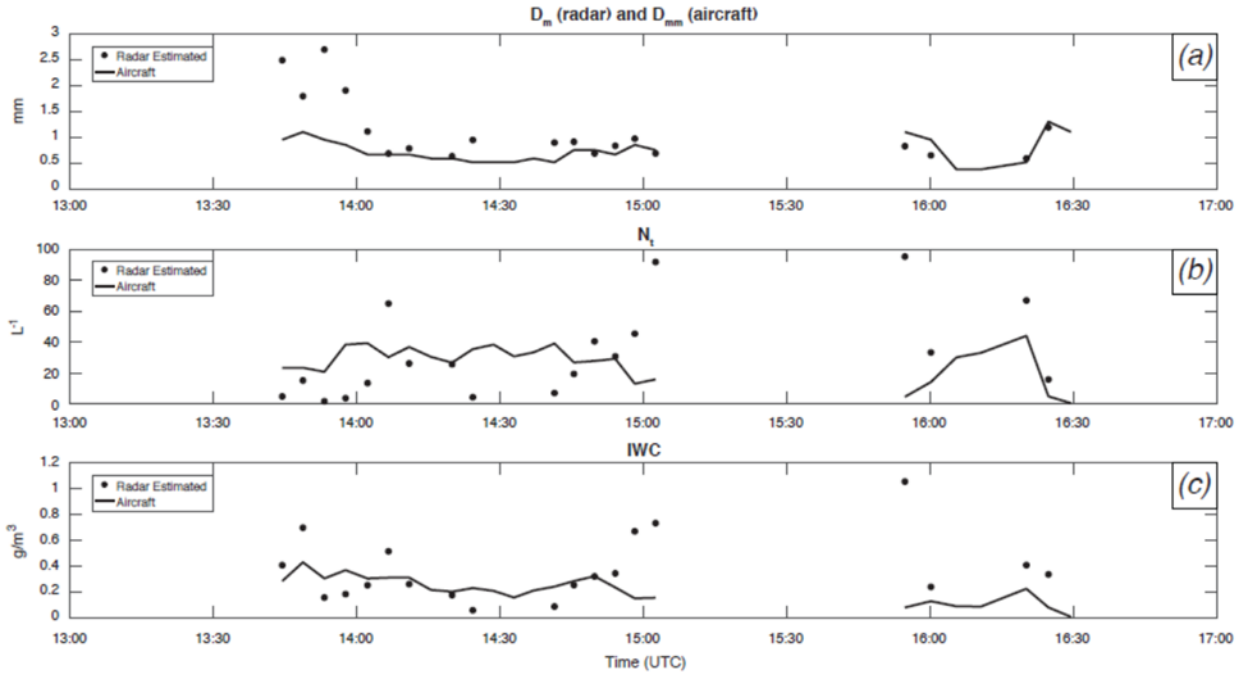

Fig. 31. Comparison of (a) mean volume diameter D_m (mm), (b) total number concentration N_t (1/L), and (c) ice water content IWC (g m^{-3}) retrieved from the polarimetric radar measurements (dots) and in situ aircraft probes (solid lines) for the MCS on 20 May 2011. From Ryzhkov and Zrnic (2019) - Fig. 11.14.

generated above the DGL has larger terminal velocity, higher K_{DP}, and lower Z_{DR} than the slower-falling anisotropic ice (e.g., dendrites or hexagonal plates) generated within the DGL.

Another area with frequent occurrence of multimodal Doppler spectra is in mixed-phase layers below the DGL, where both populations produce Z_{DR} and K_{DP} values close to 0, suggesting the impact of the aggregation and riming processes. Joint analysis of the Doppler spectra and the polarimetric radar variables provides important insight into the microphysics of snow formation and allows for separation of the contributions of ice of different habits to the values of reflectivity Z and Z_{DR}.

3.4 Statistical analysis of polarimetric radar signatures in ice / snow.

A similar physical concept, i.e., the coexistence of quasi-spherical ice falling from above and the anisotropic ice generated within the DGL, explains the results of the Griffin et al. (2018) study where the systematic analysis of the quasi-vertical profiles (QVP) of Z, Z_{DR}, and K_{DP} in the cold-season storms observed with the multiple WSR-88D radar was performed. To quantify the QVP observations within DGL, Griffin et al. (2018) computed 90th percentile maxima of Z, Z_{DR}, and K_{DP} in the DGL in five cold-season storms (Fig. 34). The data demonstrate the distinct correlations of the cloud top temperature with Z_{DR} and K_{DP} signatures in DGLs. The increase of the cloud top temperature causes apparent increase of the DGL Z_{DR} whereas K_{DP} increases for

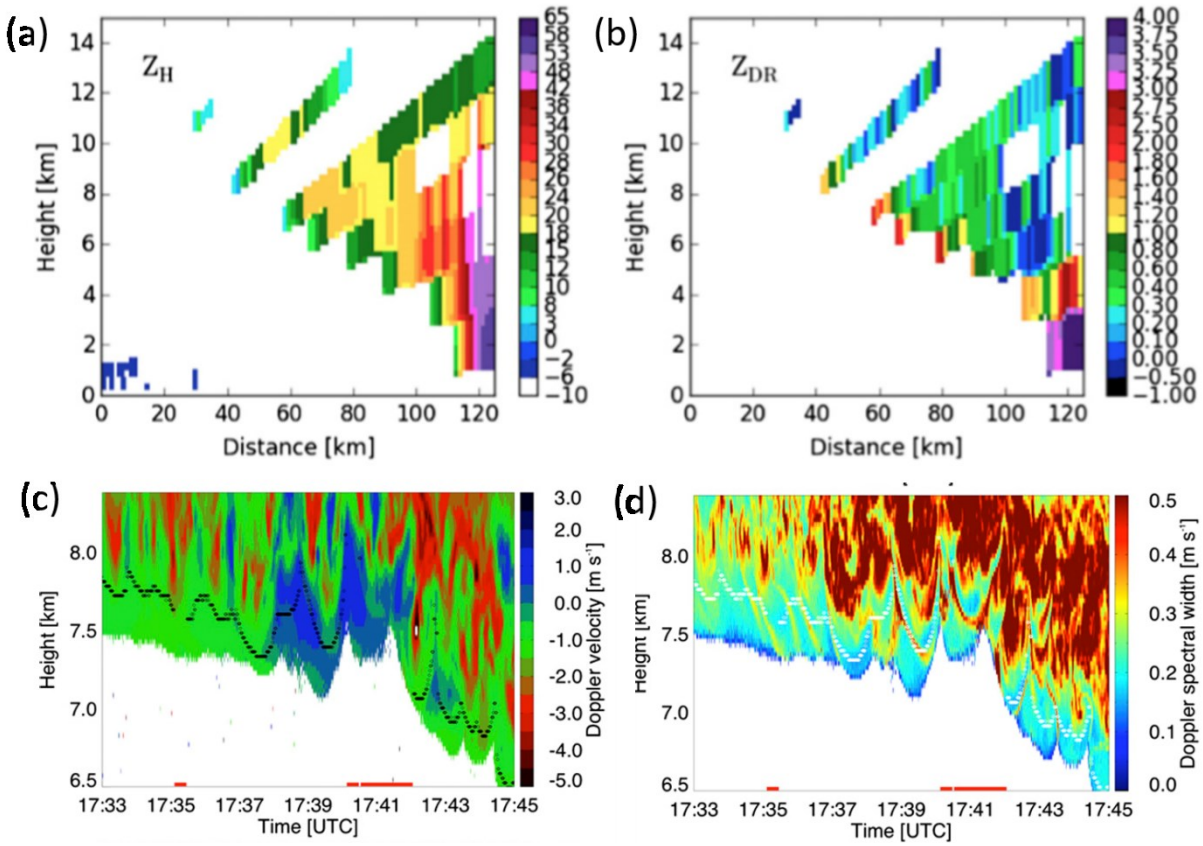

Fig. 32. Cross sections of Z (panel a) and Z_{DR} (panel b) measured by the C-band radar in the anvil of MCS on 9 June 2014 in Germany; mean Doppler velocity (panel c) and spectrum width (panel d) measured by the JOYRAD-35 Ka-band cloud radar for the same storm. Adapted from Troemel et al. (2017).

lower cloud top temperature. The statistics also show that larger Z_{DR} is associated with smaller Z in the DGL, while larger K_{DP} is usually combined with larger Z in the DGL.

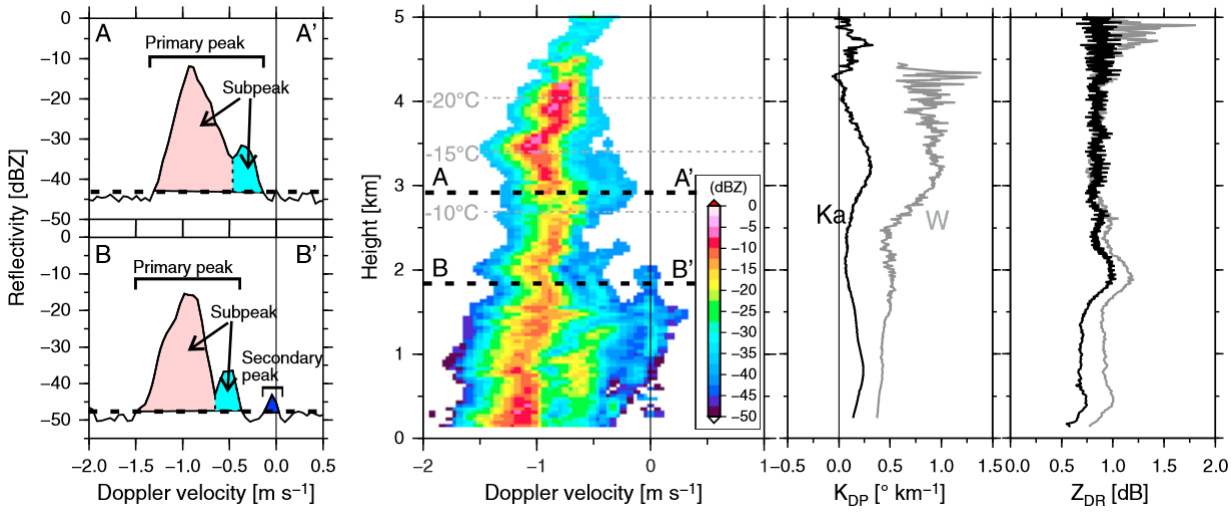

Fig. 33. (a) Example of Ka-band ARM zenith pointing radar Doppler velocity spectra showing a profile and single spectrum along A – A' and B – B'. Color shade in the profile plot represents reflectivity. Horizontal grey dashed lines represent heights of temperature of -10°C, -15°, and -20°C. (b) Quasi-vertical profiles (QVPs) of K_{DP} and Z_{DR} estimated form a Ka (black lines) and W (grey lines) SACR2 PPI scan at an elevation angle of 20°. From Oue et al. (2018).

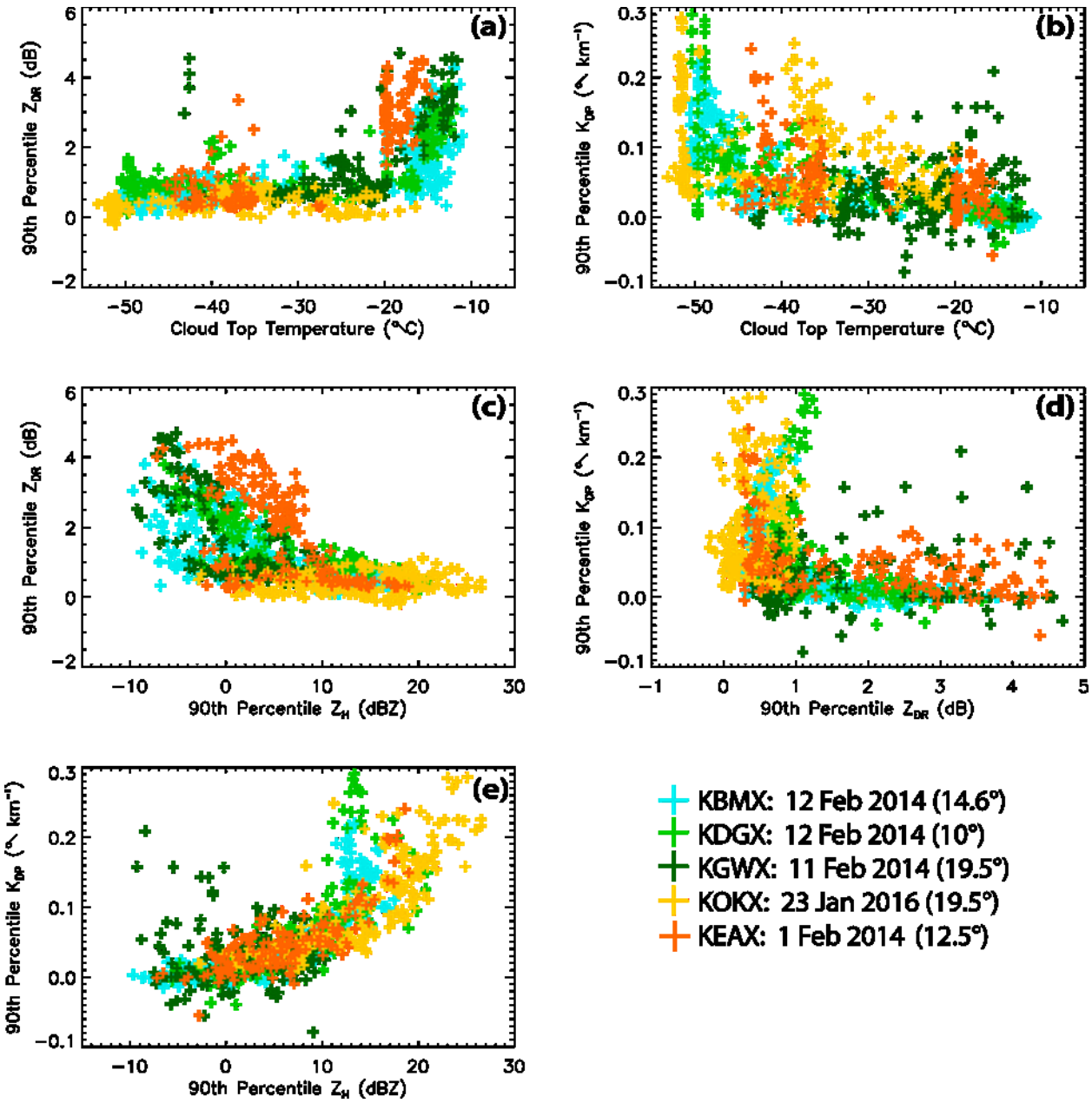

Fig. 34. Composite scatterplots of a) cloud top temperature (°C) vs. 90th percentile maximum Z_{DR} in the DGL, b) cloud top temperature (°C) vs. 90th percentile maximum K_{DP} in the DGL, c) 90th percentile maximum Z_H in the DGL vs. 90th percentile maximum Z_{DR} in the DGL, d) 90th percentile maximum Z_{DR} in the DGL vs. 90th percentile maximum K_{DP} in the DGL, and e) 90th percentile maximum Z_H in the DGL vs. 90th percentile maximum K_{DP} in the DGL. Data from the events observed with the KBMX (Birmingham AL), KDGX (Jackson MS), KGWX (Columbus OH), KOKX (Upton NY), and KEAX (Kansas City MO) WSR-88Ds are indicated by the light blue, light green, dark green, yellow, and orange symbols in each plot, respectively. Adapted from Griffin et al. (2018).

IV. Professional growth

Two PhD level graduate students (Jacob Carlin from the University of Oklahoma and Eyal Ilotoviz from the Hebrew University of Jerusalem) have been supported during the project and provided all necessary training for their professional development. Both of them successfully defended their PhD theses. Amanda Murphy, a MS level student from the University of Oklahoma, was also hired using funding from the grant. Amanda defended her MS thesis in 2018.

V. Publications

The results of research supported by the grant are published in 2 monographs and 43 journal articles.

Books:

Khain, A., and M. Pinsky, 2018: *Physical Processes in Clouds and Cloud Modeling.* Cambridge University Press, 626 pp.

Ryzhkov, A., and D. Zrnic, 2019: *Radar Polarimetry for Weather Observations*. Springer Atmospheric Sciences, 486 pp.

The monograph of Ryzhkov and Zrnic (2019) received the 2019 Atmospheric Science Librarians International (ASLI) CHOICE award for best book in the field of atmospheric science.

Journal articles:

1. Bukovcic, P., **A. Ryzhkov**, D. Zrnic, and G. Zhang, 2018: Polarimetric radar relations for quantification of snow based on the disdrometer data. *Journal of Applied Meteorology and Climatology,* **57**, 103 – 120.
2. Bühl J., S. Alexander, S. Crewell, A. Heymsfield, H Kalesse, **A.P. Khain**, M. Maahn, K V. Tricht, M. Wendisch, 2017: Remote sensing. *Meteorological Monographs* **58**, 10.1-10.21.
3. Carlin, J., **A. Ryzhkov**, J. Snyder, and **A. Khain**, 2016: Hydrometeor mixing ratio retrievals for strom-scale radar data assimilation: Utility of current equations and potential benefits of polarimetry. *Monthly Weather Review,* **144**, 2981 – 3001.
4. Carlin, J., J. Gao, J. Snyder, and **A. Ryzhkov**, 2017: Assimilation of Z_{DR} columns for improving the spin-up and forecast of convective storms in storm-scale models: Proof-of-concept experiments. *Monthly Weather Review,* **145**, 5033 – 5057.
5. Carlin, J. and **A. Ryzhkov**, 2019: Estimation of melting layer cooling rate from dual-polarization radar: Spectral bin model simulations. *J. Appl. Meteor. Clim.,* **58**, 1485 – 1508.
6. Fan J., B. Han, A. Varble, H. Morrison, K. North, P. Kollias, B. Chen, X. Dong, **S. E Giangrande**, A. **P. Khain**, Y. Lin, E. Mansell, J. A. Milbrandt, R. Stenz, G. Thompson, Y. Wang, 2017: Cloud-resolving model intercomparison of an MC3E squall line case: Part I—Convective updrafts. *J. Geophys. Res*. *Atmospheres* **122** (17), 9351-9378.
7. Fridlind, A., X. Li, D. Wu, M. van Lier-Walqui, A. Ackerman, W.-K. Tao, G. McFarquhar, W. Wu, X. Dong, J. Wang, **A. Ryzhkov**, P. Zhang, M. Poellot, A. Neumann, and J. Tomlinson, 2017:

Derivation of aerosol profiles for MC3E convection studies and use in simulations of the 20 May squall line case. *Atmospheric Chemistry and Physics,* **17**, 5947 – 5972.

8. Fridlind, A., M. van Lier-Walqui, S. Collis, S. Giangrande, R. Jackson, X. Li, T. Matsui, R. Orville, M. Picel, D. Rosenfeld, **A. Ryzhkov**, R. Weitz, and P. Zhang, 2019: Use of polarimetric radar measurements to constrain simulated convective cell evolution: A pilot study with Lagrangian tracking. *Atmos. Meas. Tech.,* **12**, 2979 – 3000.
9. Gavze E, M Pinsky, **A.P. Khain**, 2016: The orientation dynamics of small prolate and oblate spheroids in linear shear flows. *International Journal of Multiphase Flow* **83**, 103-114.
10. Griffin, E., T. Schuur, and **A. Ryzhkov**, 2018: A polarimetric analysis of ice microphysical processes in snow, using quasi-vertical profiles. *J. Appl. Meteorol. Climatol.,* **57**, 31 – 50.
11. Heiblum R**.**, O. Altaratz, I. Koren, G. Feingold, A. Kostinski, **A. Khain**, M. Ovchinnikov, E. Fredj, G. Dagan, L. Pinto, R. Yaish, Q. Chen, 2016, Characterization of cumulus cloud fields using trajectories in the center of gravity versus water mass phase space: 1. Cloud tracking and phase space description, *J. Geophys. Res. Atmos*., **121**, 6336–6355.
12. Heiblum R.., O. Altaratz, I. Koren, G. Feingold, A. Kostinski, **A. Khain**, M. Ovchinnikov, E. Fredj, G. Dagan, L. Pinto, R. Yaish, Q. Chen, 2016: Characterization of cumulus cloud fields using trajectories in the center-of-gravity vs. water mass phase space. Part II: Aerosol effects on warm convective clouds. *J. Geophys. Res*. *Atmos*., **121**, 6356–6373.
13. Hu, J., D. Rosenfeld, D. Zrnic, E. Williams, P. Zhang, J. Snyder, R. Orville, **A. Ryzhkov**, E. Hashimshoni, R. Zhang, R. Weitz, 2019: Multiple Convective Cell Identification and Tracking Algorithm for documenting time-height evolution of polarimetric radar variables and lightning properties*. Atmospheric Research,* **226,** 192 – 207.
14. Hu, J., D. Rosenfeld, **A. Ryzhkov**, D. Zrnic, E. Williams, P. Zhang, J. Snyder, R. Zhang, and R. Weitz, 2019: Polarimetric radar convective cell tracking reveals large sensitivity of cloud precipitation and electrification properties to CCN. *Journal of Geophysical Research. Atmosphere,* DOI: 10.1029/2019JD030857.
15. Ilotoviz, E., and **A. Khain**, 2016: Application of a new scheme of cloud base droplet nucleation in a spectral (bin) microphysics cloud model: sensitivity to aerosol size distribution. *Atmos. Chem. Phys*., **16**, 14317-14329.
16. Ilotoviz, E, N. Benmoshe, **A.P. Khain**, V. T.J. Phillips and **A. V. Ryzhkov**, 2016: Effect of aerosols on freezing drops, hail and precipitation in a mid-latitude storm. *J. Atmos. Sci.* **73**(1), 109-144.
17. Ilotoviz, E. and **A. Khain, A. Ryzhkov**, J. Snyder, 2018: Relationship between aerosols, hail microphysics and Z_{DR} columns, *J. Atmos. Sci.,* **75**, 1755 – 1781.
18. **Khain A**., B. Lynn and J. Shpund, 2016: High Resolution WRF Simulations of Hurricane Irene: Sensitivity to Aerosols and Choice of Microphysical schemes. *Atmos. Research*. **167**, 129–145.
19. **Khain A**., M. Pinsky and L. Magaritz-Ronen, 2018: Physical interpretation of mixing diagrams. *Journal of Geophysical Research: Atmospheres*, **123**, 529-542.
20. Khain P., R. Heiblum, U. Blahak, Y. Levi, H. B. Muskatel, E. Vadislavsky, O. Altaratz, I. Koren, G. Dagan, J. Shpund and **A.P. Khain**, 2019: Parameterization of vertical profiles of governing microphysical parameters of shallow cumulus cloud ensembles using LES with bin microphysics. *J. Atmos. Sci*., **76**, 533- 560.
21. Korolev,A., **A.P. Khain**, A., Pinsky, M., and French, J.: Theoretical study of mixing in liquid clouds – Part 1: Classical concept, *Atmos. Chem. Phys.,* 16, 9235-9254, 2016 http://www.atmos-chem-phys.net/16/9235/2016/, doi:10.5194/acp-16-9235-2016.

22. Lee H., J.-J. Baik and **A.P. Khain**, 2018: Turbulence Effects on Precipitation and Cloud Radiative Properties in Shallow Cumulus: an Investigation Using the WRF-LES Model Coupled with Bin Microphysics. *Asia-Pacific Journal of Atmospheric Sciences,* 1-15.
23. Lynn, B., **A. Khain**, J. Bao, S. Michelson, T. Yaun, G. Kelman, D. Rosenfeld, J. Shpund, and N. Benmoshe, 2016: The Sensitivity of Hurricane Irene to aerosols and ocean coupling: simulations with WRF Spectral bin microphysics. *J. Atmos. Sci*. **73**, 467-486.
24. Magaritz-Ronen L., M. Pinsky, and **A. Khain**, 2016a: Drizzle formation in stratocumulus clouds: effects of turbulent mixing. Atmos. Chem. Phys., 16, 1849–1862, 2016. doi:10.5194/acp-16-1849-2016
25. Magaritz-Ronen, L., **A. Khain**, and M. Pinsky, 2016b: About the Horizontal Variability of Effective Radius in Stratocumulus Clouds, *Journal of Geophysical Research, 121(16), DOI:10.1002/2016JD024977.*
26. Oue, M., P. Kollias, **A. Ryzhkov,** and E. Luke, and, 2018: Towards exploring the synergy between cloud radar polarimetry and Doppler spectral analysis in deep cold precipitating systems in the Arctic. *Journal of Geophysical Research, Atmosphere,* **123**, DOI: 10.1002/2017JD027717.
27. Paukert M., J. Fan, P. J. Rasch, H. Morrison, J. A. Milbrandt, J. Shpund, and **A. Khain**, 2018: Three-Moment Representation of Rain in a Bulk Microphysics Model. *J. Advances in Modeling Earth Systems* 11, 257–277.
28. Pinsky, M., and **A.P. Khain**, 2018: Theoretical Analysis of the Entrainment–Mixing Process at Cloud Boundaries. Part I: Droplet Size Distributions and Humidity within the Interface Zone. *J. Atmos. Sci*., 75 (6), 2049-2064.
29. Pinsky, M., and **A. Khain**, 2018: Theoretical analysis of mixing in liquid clouds. Part IV: DSD evolution and mixing diagrams. *Atmospheric Chemistry and Physics,* **18**, 3659- 3676.
30. Pinsky, M., **A. Khain**, A. Korolev, 2018: Theoretical analysis of liquid-ice interaction in unsaturated environment with application to the problem of homogeneous mixing. *J. Atmos. Sci.*, **75**, 1045 – 1062.
31. Pinsky M., and **A.P. Khain**, 2019a: Theoretical Analysis of the Entrainment–Mixing Process at Cloud Boundaries. Part II: Motion of Cloud Interface. *J. Atmos. Sci.*, **76**, 2599 – 2616.
32. Pinsky M. and **A. Khain,** 2019b: Analytical investigation of the role of lateral mixing in the evolution of non-precipitating Cu. Part I: Developing clouds. *J. Atmos. Sci*., https://doi.org/10.1175/JAS-D-19-0036.1.
33. Pinsky M. and **A. Khain**, 2019c: Analytical investigation of the role of lateral mixing in the evolution of non-precipitating Cu. Part II: Dissolving stage. *J. Atmos. Sci*., https://doi.org/10.1175/JAS-D-19-0118.1.
34. Pinsky M. and **A. Khain**, 2019d: Calculation of supersaturation maximum and droplet concentration at cloud base. *Atmospheric Research*. DOI:10.1016/j.atmosres.2019.104694
35. Phillips V., J. Yano and **A. Khain,** 2017: Ice multiplication by break-up in ice-ice collisions. Part 1: Theoretical formulation. *J. Atmos. Sci*., **74**, 1705 – 1719.
36. Phillips V., J. Yano, M. Formenton, E. Ilotoviz, V. Kanawade, I. Kudzotsa, J. Sun, A. Bansemer , A. Detwiler, **A. Khain** and S. Tessendorf, 2017: Ice multiplication by break-up in ice-ice collisions. Part 2: Numerical simulations. *J. Atmos. Sci.*, **74**, 2789 – 2811.
37. Shpund J., **A.Khain**, B. Lynn, J. Fan, B. Han, **A. Ryzhkov**, J. Snyder, J. Dudhia, D. Gill, 2019a: Simulating a Mesoscale Convective System Using WRF with a New Spectral Bin Microphysics - Part

1: Hail vs Graupel. *Journal of the Geophysical Research*, *Atmospheres*, **124**, https://doi.org/10.1029/2019JD030576.

38. Shpund J., **A.P. Khain** and D. Rosenfeld, 2019b: Effects of sea spray on microphysics and intensity of deep convective clouds, *J. Geophys Res*. **124**, 9484 – 9509.
39. Shpund J., **A.P. Khain** and D. Rosenfeld, 2020c: Effects of Sea Spray on the Dynamics and Microphysics of an Idealized Tropical Cyclone, *J. Atmos. Sci.*, **76**, 2213 – 2234.
40. Qu Yi, **A. Khain**, V. Phillips, E. Ilotoviz, J. Shpund, S. Patade, B. Chen, 2020: The role of ice splintering on microphysics of deep convective clouds forming under different aerosol conditions: simulations using the model with spectral bin microphysics. *J. Geophys. Res*., https://doi.org/10.1029JD031312.
41. **Ryzhkov, A**., S. Matrosov, V. Melnikov, D. Zrnic, P. Zhang, Q. Cao, M. Knight, C Simmer, and S. Troemel, 2017: Estimation of depolarization ratio using radars with simultaneous transmission / reception. *J. Appl. Meteorol. Clim.*, **56**, 1797 – 1816.
42. Troemel, S., **A. Ryzhkov,** M. Diederich, K. Muhlbauer, S. Kneifel, J. Snyder, and C. Simmer, 2017: Multisensor characterization of mammatus. *Monthly Weather Review,* **145**, 235 – 251.
43. Xie, X., R. Evaristo, S. Troemel, P. Saavedra, C. Simmer, and **A. Ryzhkov**, 2016: Radar observation of evaporation and implications for quantitative precipitation and cooling rate estimation. *J. Atmos. Oceanic Technol.*, **33**, 1779 – 1792.